Compressible Flow Structure of Droplets Under Supersonic Conditions

Eric Lin

A thesis

submitted in partial fulfillment of the

requirements for the degree of

Master of Science in Aeronautics & Astronautics

University of Washington

2013

Committee:

James C. Hermanson

Mitsuru Kurosaka

Program Authorized to Offer Degree:

Aeronautics & Astronautics

University of Washington

Abstract

Compressible Flow Structure of Droplets Under Supersonic Conditions

Eric Lin

Chair of the Supervisory Committee:
Professor James C. Hermanson
Aeronautics & Astronautics

The compressible flow structure in front of deforming droplets in a continuously accelerating supersonic flow was examined in a draw-down supersonic wind tunnel which allowed relative velocities as high as Mach 1.8. 100-μm diameter droplets were generated upstream of the tunnel entrance using a Droplet-On-Demand generator. Direct backlit and schlieren imaging were performed in order to verify the experimental configuration and image the shock structure, respectively. The test liquid employed was 2-propanol due to its non-volatile nature and ease of injection. Theoretical predictions provide a first order approximation for several bow shock parameters. The schlieren images were processed to highlight the droplet and bow shock structure. Measurements of blurred shock thickness and Mach angle were found to be generally consistent with theoretical predictions. The time scales of shock formation and shock reaction to droplet deformation were estimated to be much less than the time scale associated with droplet breakup.

Chapter 1 - Introduction

1.1 Background

The breakup and vaporization of liquid droplets in locally supersonic flow is a topic applicable, under certain conditions, to supersonic combustion ramjets (scramjets). Scramjets are currently under development by various research groups as a method to access the hypersonic flight regime. The classic limit of turbomachinery engines, such as gas turbines, that transfer energy between rotors and fluids is approximately Mach 3 due to the inefficiency of the gas turbine cycle at higher Mach numbers. By replacing the rotary components with an intake that uses dynamic air pressure to increase static air pressure inside the engine, a process known as ram air ingestion, it is possible to reach speeds of Mach 5. In ram air ingestion, supersonic air is slowed to subsonic speeds before being fed into the combustor. However, as Mach number increases, the stagnation temperature of the incoming air increases accordingly. In the hypersonic regime, typically defined as Mach 5 and above, the incoming air has such a high stagnation temperature that it is no longer possible to raise the static temperature of the air through addition and combustion of fuel, and therefore subsonic combustion becomes infeasible.

The scramjet is a variation of the ramjet in which the actual combustion takes place in supersonic flow. By allowing combustion under supersonic conditions, the limitation of ramjets is removed as the static temperature of the air remains relatively low and can be significantly increased through addition and combustion of fuel. Major recent scramjet-development programs have included the X-43 and X-51.

While scramjets have successfully broken the hypersonic regime, supersonic combustion raises additional problems; primarily, the fuel must be injected, mixed with air, ignited, and burned within a millisecond time frame. Traditionally, scramjet combustion has employed hydrogen fuel. Hydrogen has several favorable traits including a higher reaction rate and shorter

ignition delay times compared to hydrocarbon fuels [1,2]. Despite the advantages that hydrogen offers, there are significant disadvantages that warrant revisiting hydrocarbon fuels. These shortcomings include low energy density and the need to be cryogenically cooled to remain in a liquid state, which can also create hazardous handling conditions and increase costs.

The higher energy density and standard storage conditions associated with liquid hydrocarbon fuels allow for less structural mass given the reduced volume required for the fuel. The longer ignition times have been addressed by pre-heating the fuel and injecting fuel in a vapor phase. However, in some situations, such as a "cold start" in which the fuel would not be pre-heated, hydrocarbon fuel may be injected while still in liquid phase. In this case, the rates and physical mechanisms associated with the injection of liquid droplets under supersonic conditions may become critical issues that may affect scramjet performance. The use of unheated fuel may however offer an advantage in that the higher momentum of liquid fuel upon injection can result in deeper penetration into the supersonic flow [3].

1.2 Droplet Parameters

The two primary parameters pertaining to droplet disruption are the Weber number (*We*) and the Ohnesorge number (*Oh*). The Weber number is a non-dimensional parameter that is often used in analyzing fluid flows when an interface between two different fluids exists. In this context, Weber number governs the mode of deformation and fragmentation of a droplet. The Weber number is defined as:

$$We = \frac{\rho_\infty v_r^2 d_o}{\sigma} \qquad \text{Equation 1.1}$$

where ρ_∞ represents static density of the incoming flow, v_r is the flow velocity relative to the droplet, d_o is the initial droplet diameter, and σ is the surface tension of the droplet. Therefore the

Weber number depends on the flow conditions and represents the importance of the incoming fluid's inertia compared to the droplet's surface tension.

The second primary parameter is the Ohnesorge number. The Ohnesorge number is another non-dimensional number which is defined as:

$$Oh = \frac{\mu_d}{\sqrt{\rho_d \sigma d_o}} \qquad \text{Equation 1.2}$$

where μ_d is the viscosity of the droplet, ρ_d is the density of the droplet, σ is the surface tension of the droplet, and d_o is the initial droplet diameter. The Ohnesorge number relates the viscous forces to inertial and surface tension forces. Unlike the Weber number, the Ohnesorge number is not dependent on flow conditions, but rather only on the fluid properties. Based on research by Krzeczkowski [4], when Ohnesorge number is greater than 0.032 the effect of viscosity droplet lifetime is negligible. However, Hirahara & Kawahashi [5] found that as the Ohnesorge number increases, the increasing importance of viscosity does increase the Weber number ranges for the onset of different breakup regimes. Generally, as long as the Ohnesorge number is less than 0.1, the effects of viscosity are negligible.

A third parameter that is used to characterize droplet motion is the Stokes number. The Stokes number is a non-dimensional parameter describing the behavior of particles in a fluid flow. More specifically, it is the ratio of the stopping distance of a droplet relative to an obstacle, and is calculated as follows:

$$Stk = \frac{\tau U_o}{d_c} \qquad \text{Equation 1.3}$$

where τ is the characteristic response time of the particle, U_o is the velocity of the flow away from the vicinity of the droplet, and d_c is a characteristic length scale. A Stokes number much greater than unity is desired in this investigation as that indicates that the droplets will be

relatively unaffected by a flow velocity change, leading to a significant lag time which can result in supersonic relative Mach numbers.

It is also important to consider the thermal behavior of the droplet, given the significant drop in static temperature that occurs in supersonic flow. The temperature change within the droplet can be described through the Fourier number, which is calculated as follows:

$$Fo = \frac{4\alpha t}{{d_o}^2} \qquad \text{Equation 1.4}$$

where α is the thermal diffusivity and t is the total time droplets are exposed to cold static temperatures, defined as more than 1 Kelvin below ambient. Physically, the Fourier number is a ratio of the heat conduction rate to the rate of thermal energy storage. It is possible that the droplet temperature will increase in supersonic flow due to viscous heating from the rapid deformation [6].

Another aspect that may affect droplet breakup behavior and vaporization is degree superheating of the droplet liquid [7]. Superheat can be defined as the ratio of vapor pressure to freestream pressure.

$$S = \frac{P_{vapor}}{P_\infty} \qquad \text{Equation 1.5}$$

The degree of superheat represents the volatility of a fluid. Also, note that there is a critical degree of superheat beyond which the fluid becomes thermodynamically unstable.

Additional parameters used to characterize the flow surrounding the droplet are the relative Mach number and the Reynolds number. The relative droplet Mach number is defined as follows [8]:

$$M_r = \frac{v_\infty - v_d}{a_\infty} \qquad \text{Equation 1.6}$$

where v_∞ is the velocity of the supersonic flow, v_d is the velocity of the droplet, and a_∞ is the speed of sound at the droplet location.

The Reynolds number is used to characterize the flow field around the droplet as well as the droplet drag. The Reynolds number is defined as:

$$Re_d = \frac{\rho_\infty v_r d_o}{\mu_d} \qquad \text{Equation 1.7}$$

where ρ_∞ is the density of the flow, v_r is the relative velocity, d_o is the droplet diameter, and μ_d is the dynamic viscosity. The Reynolds number expresses the ratio of the inertial forces to viscous forces and consequently, determines the importance of these two types of forces.

Finally, the Knudsen number of the flow can be important. Knudsen number is a dimensionless parameter that compares the length of the mean free path to a characteristic length scale. The Knudsen number can be related to the Mach number and the Reynolds number as follows:

$$Kn = \frac{M}{Re}\sqrt{\frac{\gamma\pi}{2}} \qquad \text{Equation 1.8}$$

If the Knudsen number is greater or equal to unity, then means the mean free path is on the order of the characteristic length, so the flow cannot be considered a continuum and rarefied gas dynamics must be used. In summary, the relevant parameters to this research are the Weber number, Ohnesorge number, Stokes number, Fourier number, degree of superheat, relative Mach number, Reynolds number, and Knudsen number, with the Weber number, relative Mach number, and degree of superheat being the most important.

1.3 Disruption of Droplets in Shock Tubes

Droplet disruption and breakup has often been previously studied in subsonic, near-sonic, and supersonic flows through the use of shock tubes. While shock tubes are capable of producing locally supersonic conditions, this involves the passage of a shock wave through the droplet. Compared to a situation where a droplet is injected into a continuously accelerating supersonic stream (the configuration employed in this research), the fundamentally different flow conditions associated with the shock-tube technique can reasonably be expected to lead to different breakup modes.

Droplet deformation and breakup modes in the comparatively steady flow created using shock tubes have been well documented and characterized based on Weber number. The breakup modes are characterized below in Fig. 1.1 [9]. The first and lowest range of Weber numbers is between 0 and 12. In this range, the droplet breakup is characterized by the droplet flattening perpendicularly to the flow and in some cases, vibrating. The next regime is for Weber numbers between 12 and 50; in this range, droplets still initially flatten perpendicularly to the flow, but the middle gradually forms into a bag, hence the name "Bag Breakup." This bag will tear into a mist, and the rim follows similarly afterwards. The following breakup regime is for Weber numbers in between 50 to 100; again, droplets form a "bag" after flattening but now, there is a structure in the center of the bag. This structure is commonly referred to as a "stamen" due to its flowerlike appearance. For droplets with Weber numbers between 100 and 350, the droplets first flatten but instead of deforming into a bag shape, these flattened droplets will continually shed fluid from their perimeter until the droplets are entirely fragmented. The final mode of droplet deformation occurs for Weber numbers greater than 350. Droplets in this range experience catastrophic

breakup where a flattened droplet pinches and strips in many places before fragmenting completely.

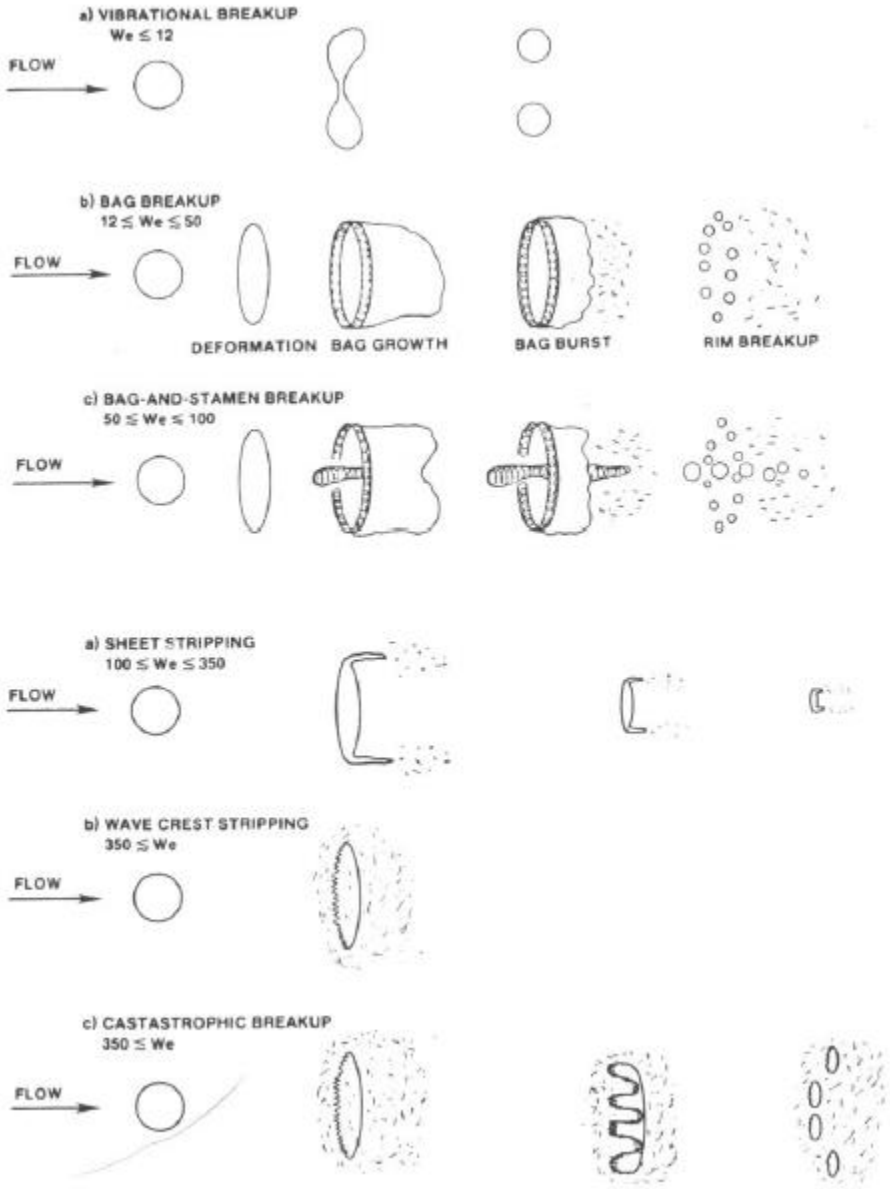

Figure 1.1 Summary of droplet breakup modes [9].

As mentioned above, the experiments discussed above were conducted primarily in shock tubes which have several differences compared to a smoothly accelerated droplet. Among these differences are the passage of a shock wave through the droplet, that the relative velocity of the

droplets remains subsonic and essentially constant due to minimal displacement of the droplet during the test, and that the test conditions do not simulate the acceleration typically experienced when a droplet is injected into a combustor. For these reasons, a method that smoothly accelerates droplets to relative supersonic Mach numbers is needed.

1.4 Disruption of Droplets in Wind Tunnels

By using a wind tunnel that smoothly accelerated droplets to relatively supersonic speeds, different test conditions can be achieved than for the case of shock tubes. This different approach to achieving supersonic conditions can allow for superheating of fluid not possible given the static rise associated with shock tubes, provided the local static pressure is lower than the vapor pressure. Droplets that are smoothly accelerated to relative supersonic Mach numbers without a shockwave passing through them has been studied by Kim & Hermanson [7,8,10] using a small scale draw-down wind tunnel with an optimal contraction profile to prevent premature droplet breakup. This configuration produced a maximum relative Mach number of 1.8. The following results based on that work are separated into four different regions along the centerline of the wind tunnel based on the nature of droplet disruption. The regions are as follows:

Region I – Deformation		The droplet is deformed, but no separation of liquid from the droplet occurs
Region II – Initial Breakup		Disruption begins; there is initial separation of liquid from the droplet and the droplet exhibits several legs
Region III – Primary Breakup		A major and increasing fraction of liquid is separated from the droplet
Region IV – Total Breakup		The droplet fragments and experiences catastrophic breakup

The table below summarizes and compares the shock tube and draw-down wind tunnel test configurations.

	Shock tubes	Supersonic accelerating flow
Flow velocity	Very large, impulsive initial acceleration to a constant velocity	Continuous acceleration of the flow throuout the domain ($M_r > 1$) This condition allow for simulating scarmjet situations more closely
Flow characteristics	Depends on the shock tube conditions including the pressure difference as well as the gases in the driver and driven section	Supersonic under-expanded jet with continuously varying flow properties
Aerodynamic loading on droplet	Impulsive aerodynamic loading at the moment of shock passage	Smoothly accelerated droplet not influenced by shock passage
Breakup mechanism	Various Weber numbers identified with different modes of breakup, **Weber number nearly constant**	At low Weber numbers, droplet deformation without breakup At high Weber numbers, the similar breakup mode to shock tube **Weber number continuously changing**
	We < 100 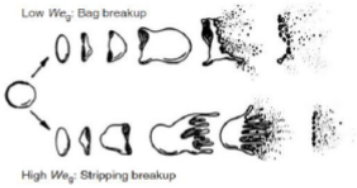 We > 100	Weber number increases  5 < We < 316
Potential superheat effects	No, static pressure rises due to shock	Yes, if the local static pressure is lower than liquid vapor pressure

Table 1.1 Comparison of shock tube and draw-down wind tunnel results [8].

The primary difference found between the shock tube and draw-down wind tunnel configuration is that droplets disrupted in the wind tunnel, where the Weber number continuously increased, were observed to disrupt an order of magnitude faster than found in similar shock tube conditions [7,8,10]. Additionally, it was found that for volatile fluids injected into a continuously accelerating flow, the droplet breakup was accelerated, contrast the results reported by Hermanson [11], where no noticeable superheating effect was observed. However, that experimental configuration resulted in higher relative Mach numbers (3.5 compared to 1.8), so a higher pressure rise behind a stronger bow shock as well as test liquids with lower vapor pressures could explain the different superheat effects. Neither experiment was however able to visualize and capture the bow shock in front of the disrupting droplet.

1.5 Research Objectives

The work presented here expands on previous research into droplets smoothly accelerated to locally supersonic Mach numbers without the passage of shock waves through the droplets. The primary focus of this research was to verify the existence of bow shocks in front of the droplet and determine their characteristics. To the extent of the author's knowledge, no one has successfully captured and imaged a bow shock in front of a droplet under these conditions. By verifying the existence of bow shocks, a better description of the flow conditions around the droplet can be gained and used to explain droplet breakup characteristics.

The objectives of this research attempt to address the following issues and questions relating to the background information presented above. More specifically:

- Do bow shocks exist in front of droplets on this scale? If so, what is the structure of the bow shocks? Are the physics the same at this scale or do viscous effects become important given the low Reynolds number?
- How does the bow shock structure change with droplet deformation?
- Are the bow shocks consistent with that expected for these flow conditions in terms of standoff and limiting Mach angle?

Chapter 2 – Experimental Setup

The primary goal of the experimental setup is to generate droplets and accelerate them smoothly to speeds that are supersonic relative to the air flow without a shockwave passing through. The setup consists of a small-scale supersonic wind tunnel to provide supersonic flow, a droplet-on-demand generator, and optical diagnostics.

(a) (b)

Figure 2.1 (a) and (b) Different views of the lab setup. The supersonic wind tunnel is at the center of (b).

2.1 Draw-down Wind Tunnel

Supersonic flow is achieved by using a draw-down wind tunnel. This produces a two dimensional (2-D) under-expanded jet configuration. Air flow is generated by evacuating a 2.8 m^3 vacuum tank with two parallel vacuum pumps (total pumping capacity of 0.5 m^3/min) in order to create a nominal backpressure of 16.7 kPa. The pressure difference causes atmospheric air to enter the draw-down wind tunnel at a stagnation temperature and pressure of T_o=293.7 K and P_o=101.3 kPa. This airflow is smoothly accelerated through a convergent nozzle before entering the test section.

The convergent nozzle was designed to prevent droplet breakup before the droplets reached a relative supersonic speed. In order to achieve this, the air flow velocity is kept as low

as possible in the subsonic section of the nozzle due to the fact that, by definition, Weber number is quadratically related to relative velocity. The desired area ratio as a function of z is given as [8]:

$$\frac{A(z)}{A_{throat}} = \frac{1}{A_{throat}}(1908z^4 - 19.8z^3 + 0.614z^2 + 1.68x10^{-3}z + 1.94x10^{-5}) \quad \text{Equation 2.1}$$

Both a 3-D and 2-D nozzle following the area ratio given above were constructed and tested. It was experimentally determined that a 2-D nozzle would suit this research better; the primary advantage of a 2-D nozzle is its transparent sidewalls which allow an unimpeded view of the droplet throughout the entire flow path, while the 3-D nozzle only allow optical access in the test section. The test section itself is made out of optical grade borosilicate glass (MIL-G-47033 grade) that is 63.5 x 63.5 mm and 6.35 mm thick. The final configuration is shown below.

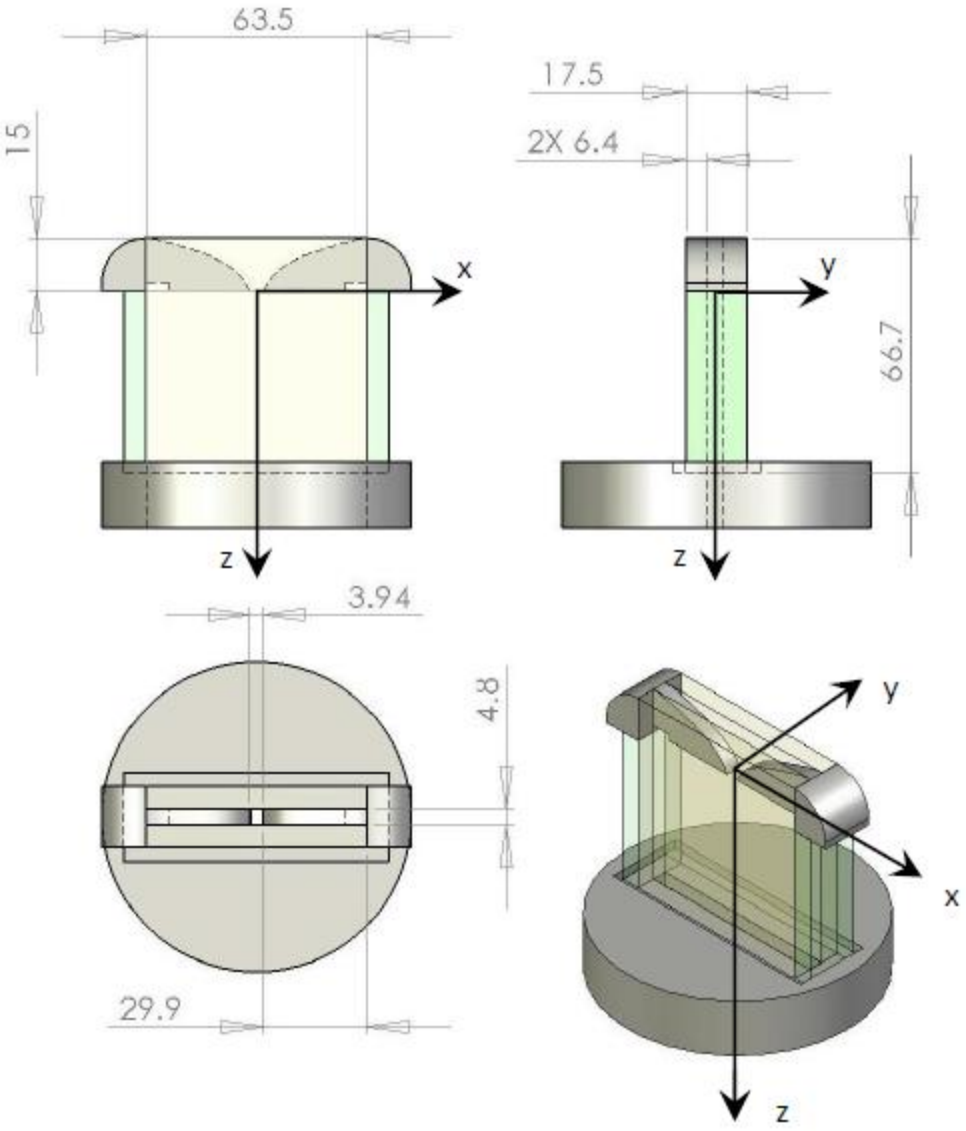

Figure 2.2 Final wind tunnel design [10].

This configuration produces a Weber number range of 5 to 316 and a maximum relative Mach number of 1.8 in a smoothly accelerated flow. The maximum Reynolds number expected is 1,400. Using Eq. 1.8, it was determined that the Knudsen number is on the order of 4×10^{-4}, which is significantly less than unity, meaning standard continuum equations apply. The Fourier number for this experiment has been calculated to be approximately 0.027; this low value suggests that the bulk of the droplet mass will be unaffected by any temperature changes.

Additionally, calculations performed by Kim & Hermanson [10] based on the temperature and static pressure in the test section, show that the droplets in the current study may be superheated but do not reach the critical limit where the fluid becomes thermodynamically unstable.

2.2 Droplet-on-Demand Generator

A droplet-on-demand (DoD) generator was used to generate droplets with the desired diameter of 100 ± 5 μm. Droplets of this size maintain a low Weber number which prevents premature droplet breakup in the subsonic region of the wind tunnel but are large enough that they lag the flow and reach a supersonic relative velocity in the supersonic region of the wind tunnel [8]. Because the Stokes number for this configuration is 49 to 86, the droplet remains relatively unaffected by changes in the flow velocity, allowing for supersonic Mach numbers relative to the droplet.

The two commonly used types of DoD devices are thermally-actuated devices and piezeoelectric devices. In thermally-activated devices, there is a fluid-filled nozzle with an embedded heater. Droplets are ejected from the nozzle by creation of vapor across the top of the heater. In a piezoelectric device, a piezoelectric transducer is embedded rather than a heater. The transducer is triggered by sending a voltage pulse. This voltage pulse causes the transducer to flex, which in turn causes an acoustic wave that creates a single droplet per pulse. Both are proven technologies capable of delivering the desired droplet size but for this research, the piezoelectric device was chosen over a thermally-actuated device to avoid the possibility of heating the fluid, which could influence the final results.

The DoD generator used in this research is a *MJ-AB* jetting device (shown below) manufactured by *MicroFab Technologies*. The DoD generator selected has a 60 micron tip and a piezo-electric actuator located within the device that is operated an a frequency of 6,000 Hz.

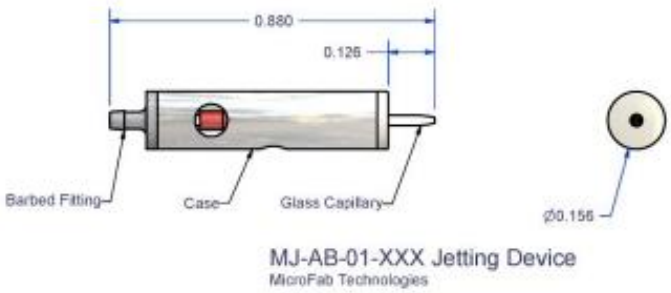

Figure 2.3 Schematic of the droplet-on-demand generator.

The *MJ-AB* jetting device is controlled through the *MicroJet III* controller. As described above, the *MicroJet III* controller sends a voltage pulse to the piezoelectric transducer in the jetting device. The ideal waveform parameters will result in spherical droplets of the desired size and no satellite droplets. A software interface supplied by *MicroFab Technologies* is used to determine and vary the piezoelectric pulse sent from the controller to the jetting device. The software interface is shown below in Fig. 2.4. The final droplet parameters that were used for the research are: a rise and fall time of 5 μs, a dwell time of 125 μs, an operating frequency of 6,000 Hz, a voltage rise of 20.0 V, and a driving pressure of 7.0 kPa. The details of how these operating conditions were determined are provided in Appendix A.

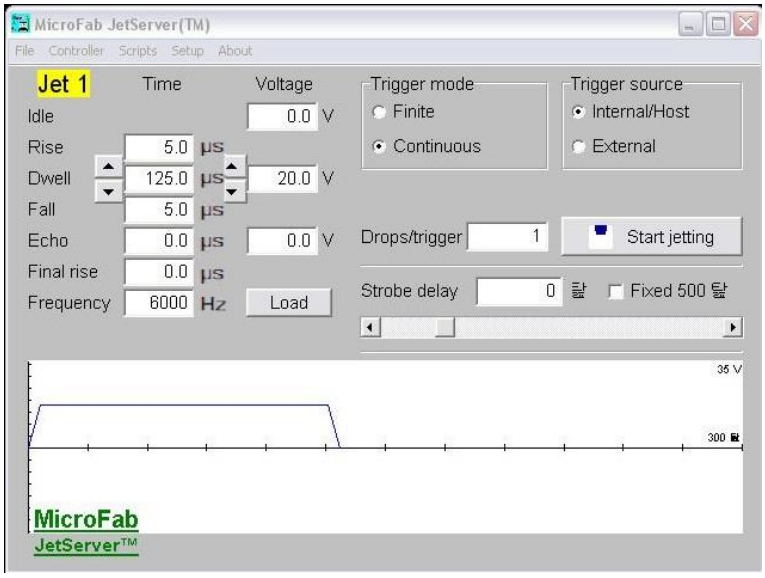

Figure 2.4 Screen capture of software interface for DoD generator.

The final component of the droplet generation system is the pressurized test liquid reservoir. The test liquid is contained in a syringe that is pressurized with nitrogen gas. The exact pressure in the syringe is determined through a combination of negative hydrostatic pressure, controlled by changing the height of the syringe relative to the jetting device, and positive nitrogen gas pressure, controlled through a pressure control system. The pressure control system, shown below, allows for adjustments in two modes, course and fine; course adjustment is used to fill the reservoir and fine adjustment (accurate to 0.2 kPa) is used to control droplet jetting once the reservoir is filled.

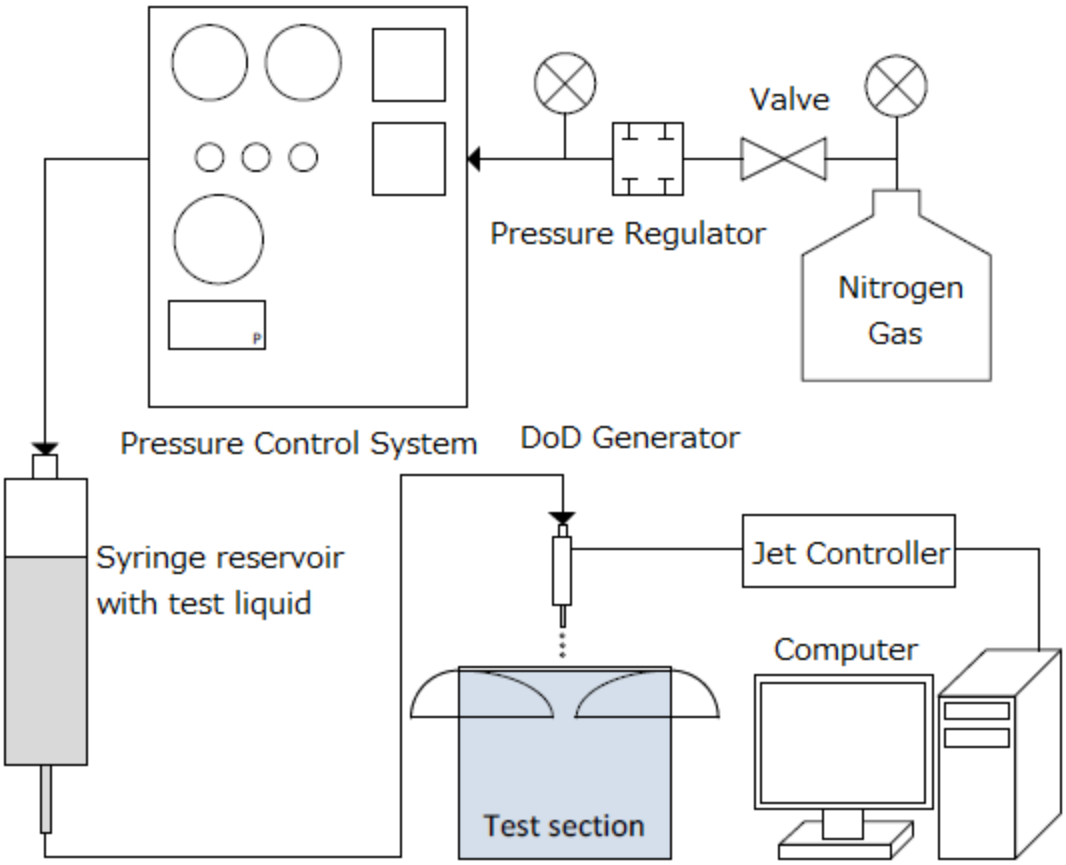

Figure 2.5 Schematic overview of the pressure control system [10].

2.3 Imaging Hardware

The nature of this research creates a unique and challenging imaging environment; it was necessary to capture a relatively frozen image in order to avoid blurring the droplet and bow shock which requires a fast exposure time. A 90 ns exposure time will result in the droplet moving approximately 4.5 μm to 11.7 μm as the image is recorded, depending on the velocity of the droplet. Additionally, a high level of magnification was required in order to actually capture a 100 μm droplet and reveal the details of disruption. The fast exposure time, magnification, and knife edge in the schlieren setup all reduced the amount of light that reaches the camera sensor. For this reason, an intensified charge-coupled device (ICCD) was needed.

The camera used in this research presented was a *PI-MAX2* System composed of a camera head and a ST-133 controller, both manufactured by *Princeton Instruments*. The *PI-MAX2* has a TH 512x512 resolution sensor and is capable of 500 ps gate times. The *PI-MAX2* was used in conjunction with a *Computar* video zoom lens capable of up to 6x zoom. In order to increase the magnification range, a series of extension tubes was used. After magnification, each pixel corresponded to approximately 10.5 microns.

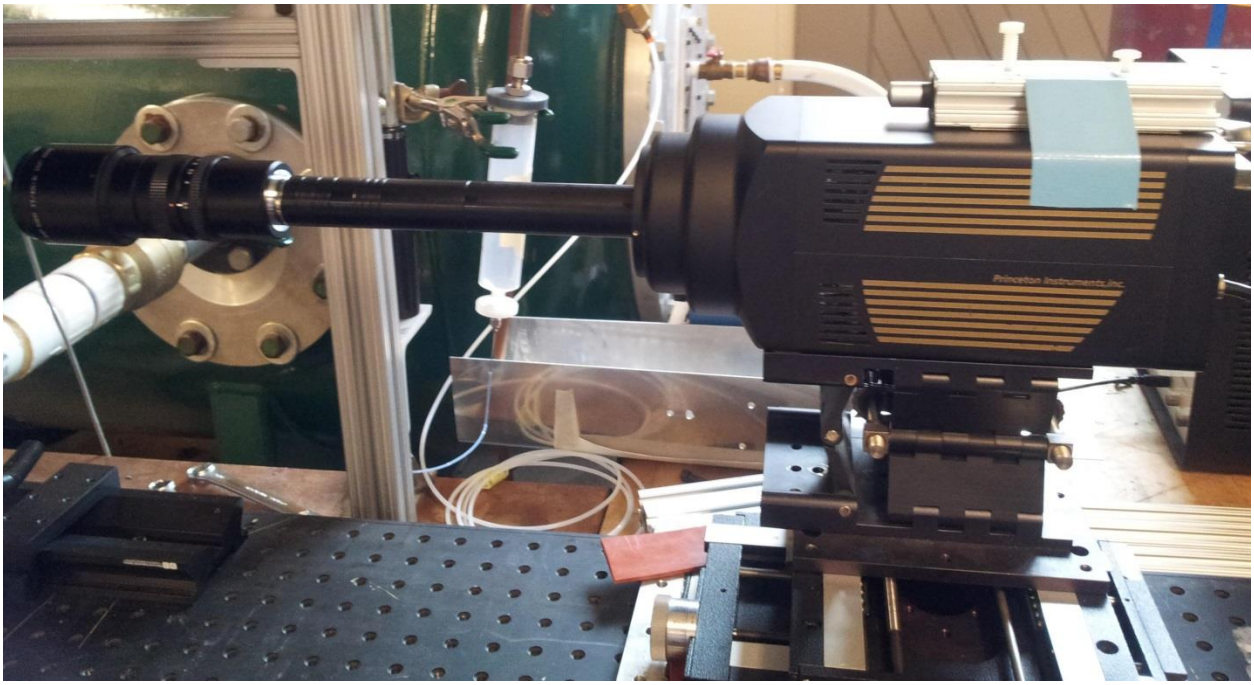

Figure 2.6 Imaging hardware mounted on an adjustable 3D stage. The *PI-MAX2* camera is visible to the right; the magnification hardware to the left.

2.4 Image Verification

In order to verify system operation and that the captured droplets, disruption behavior, and flow conditions are similar to those previously employed, direct backlit images were taken using the *PI-MAX2* system, *Computar* zoom lens, and the extension tubes using the same exposure settings that would be used later in the schlieren imaging. The images were processed as follows. First, a general region around the droplet was selected. Then the contrast of this

region was adjusted until both the droplet and bow shock are visible. Noise was reduced by replacing pixels with the mean value of neighboring pixels if they exceed that mean value by a certain threshold. Finally, the background of the image was erased in order to highlight the droplet and bow shock. The figure below demonstrates the image processing method.

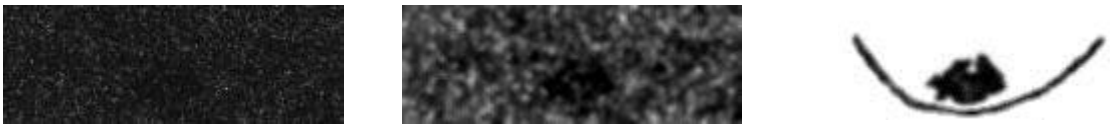

(a) Raw Region (b) Contrast Adjusted (c) Background Subtracted

Figure 2.7 Demonstration of the image processing method.

A sample of the verification images are shown below for the various deformation regions. The approximate extent of each region is stated as determined by Kim & Hermanson [8,10].

Deformation Region	Current Research	Previous Research [8,10]
Region I z = -12 to -2 mm		
Region II z = -2 to 0 mm		
Region III z = 0 to 3 mm		
Region IV z = 3 to 6.5 mm		

Table 2.1 Comparison of backlit images from current and previous research.

While the images taken with the *Computar* lens are not as clear as the images from previous research, the shape and deformation of the suspected droplets correspond closely to deformations captured in previous experiments. The somewhat lower image quality is likely due to a combination of several factors, such as using a different lens, different magnification levels, using a different light source, and using different exposure times. In any case, it is clear that droplets following the same deformation modes are being captured.

2.5 Schlieren System

In order to visualize the expected bow shocks in front of the droplets, schlieren imaging was employed. A schlieren system collimates light from a point source so that any density gradients that exist in the flow will deflect the collimated light due to variations in the index of refraction. The distorted light is then focused imperfectly and a knife-edge is used to block a portion of the light. This creates light and dark patches in the resulting image that correspond to the density gradients.

The schlieren system used in this research is a single-pass system. An *ORIEL* 68806 arc lamp with a xenon bulb capable of producing 1,000 lumens is used as a continuous light source. The light is collimated by a 25.5" focal length mirror and directed at the test section before being focused by a 40x250mm lens. The camera itself is located behind the knife edge, which is located at the focal point of the 40x250mm lens. The schlieren system is shown below in Fig. 2.8 and images of the under-expanded jet are shown in Fig. 2.9 (a) and (b).

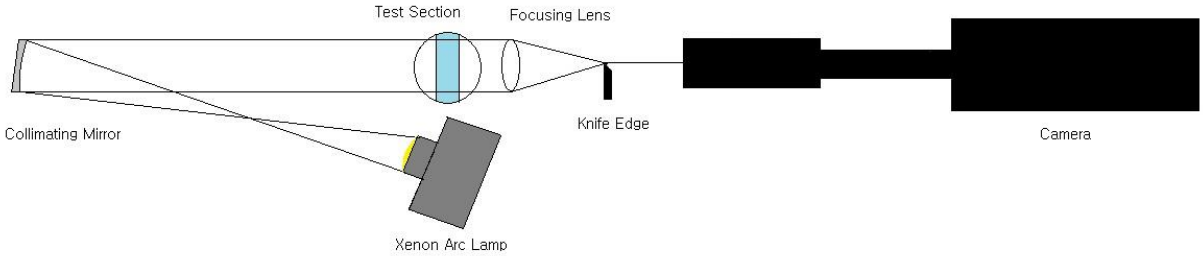

Figure 2.8 Schematic drawing of the schlieren setup.

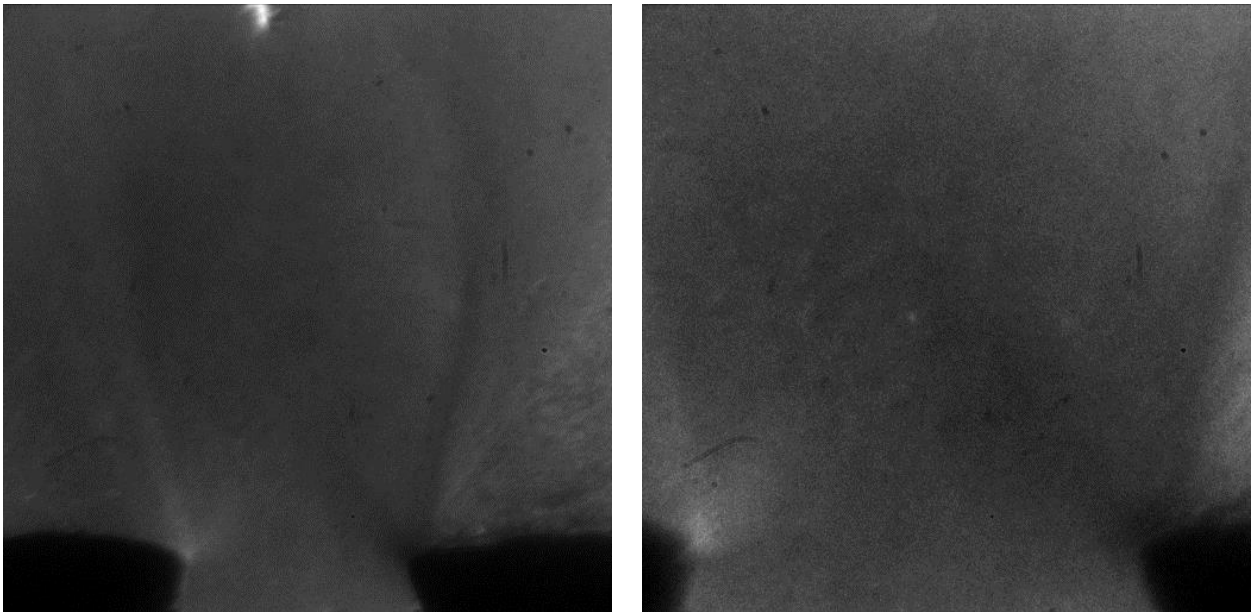

(a) (b)

Figure 2.9 (a) and (b) Under-expanded jet at two different levels of magnification.

Chapter 3 – Results and Discussion

3.1 Theoretical Predictions for Bow Shock Characteristics

Due to the comparative lack of experimental literature on the compressible flow structure in the vicinity of supersonic droplet of this size, theoretical predictions are needed to provide an estimate of the bow shock characteristics, such as thickness, standoff distance, shock formation time, and shock reaction time. The primary methods that will be used for estimating bow shock characteristics are the method of characteristics and the Mott-Smith solution to the Navier-Stokes equations, both of which have been experimentally verified, albeit for structures much larger than the droplets considered here.

The bow shock thickness was predicted through the Mott-Smith solution. Mott-Smith reasoned that the distribution function within the shock can be treated as a weighted sum of upstream and downstream distribution functions. The distribution functions are a statistical function describing the concentration of a quantity per unit volume as a function of space. Additionally, the fluxes of mass, momentum, and energy are taken to be constant within a shock wave. By combining these observations, Mott-Smith derived an approximate solution that satisfied the conservation equations. The Mott-Smith solution is as follows [12]:

$$\frac{u-u_\beta}{u_\alpha-u_\beta}=\{1+\exp[(1-\frac{u_\beta}{u_\alpha})\frac{x}{A\lambda_\alpha}]\}^{-1} \qquad \text{Equation 3.1}$$

with

$$A\equiv\sqrt{\frac{2}{\pi}}\frac{u_\beta}{u_\alpha}[\left(1-2\frac{u_\beta}{u_\alpha}\right)\frac{u_\alpha}{\sqrt{kT_\alpha/m}}+3\frac{\sqrt{kT_\alpha/m}}{u_\alpha}]$$

where u is the flow velocity, x is the distance within the shock structure, λ is the mean free path, k is the Boltzmann's constant, T is the temperature, α represents the region upstream of the shock, and β represents the region downstream of the shock. The density-gradient thickness was

calculated using the Mott-Smith solution and compared to experimental data. A plot of dimensionless density-gradient thickness versus Mach number is shown below, where the solid line is the Mott-Smith solution and the circular points are experimental results:

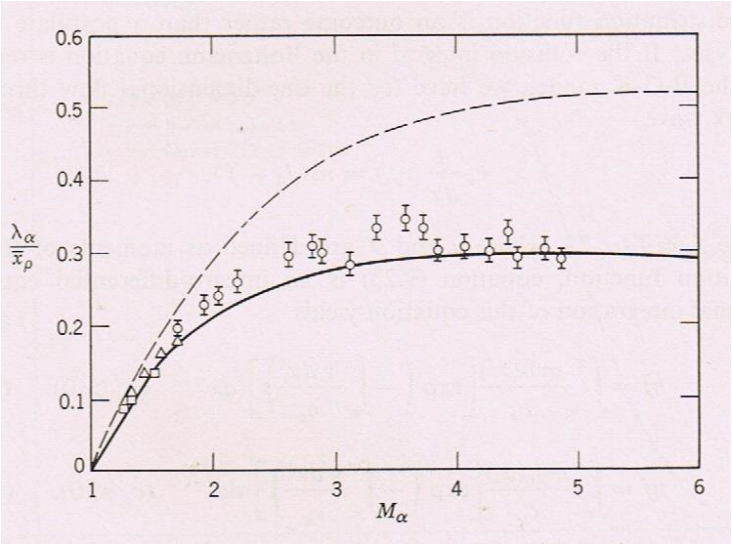

Figure 3.6 Plot of the Mott-Smith solution and experimental data [12].

In Fig. 3.6, λ_α represented the mean free path upstream of the shock, x_ρ represents the thickness of the density gradient and M_α represents the Mach number upstream of the shock. As shown above, the Mott-Smith solution is most accurate for Mach numbers in between 1 and 2 and for Mach numbers greater than 3.5. Therefore the Mott-Smith solution and bow shock thickness estimates based it are applicable to this research given that the highest relative Mach number achieved is 1.8. Based on this solution, a bow shock thickness of 6 to 50 times the freestream mean free path (240 nm to 2,000 nm) can be expected, depending on the relative Mach number with lower Mach numbers resulting in thicker bow shocks.

In order to approximate the shock formation time and standoff distance, the method of characteristics is used. The characteristic technique is essentially an exact solution to the governing equations which are conservation of mass, momentum, and energy. The limiting factor for the accuracy of the characteristic technique is the resolution with which the

characteristics are draw. Mann [13] has thoroughly worked out a one-dimensional solution for an accelerating piston, which will be taken as representing a rough approximation of the bow shock development on the droplet centerline. This solution is computationally based on the Riemann variables, as is usually the case for the method of characteristics. The Riemann variables are as follows:

$$P \equiv \frac{2}{\gamma - 1} A + U \qquad \text{Equation 3.2}$$

and

$$Q \equiv \frac{2}{\gamma - 1} A - U \qquad \text{Equation 3.3}$$

where *P* represents the path of the wave moving in the same direction as the piston, *Q* represents the path of the wave moving in the opposite direction, γ represents the ratio of specific heats, and *U* and *A* are dimensionless flow velocity and speed of sound. By taking the derivatives of Equation 3.2 and 3.3, the physical characteristics can be defined as:

$$\frac{d\xi}{d\tau} = U + A \qquad \text{Equation 3.4}$$

$$\frac{d\xi}{d\tau} = U - A \qquad \text{Equation 3.5}$$

Here, ξ and τ are dimensionless distance and time while *U* and *A* are still dimensionless flow velocity and speed of sound. Figure 3.7 below is a dimensionless plot of time and distance where piston and wave paths are shown [13]:

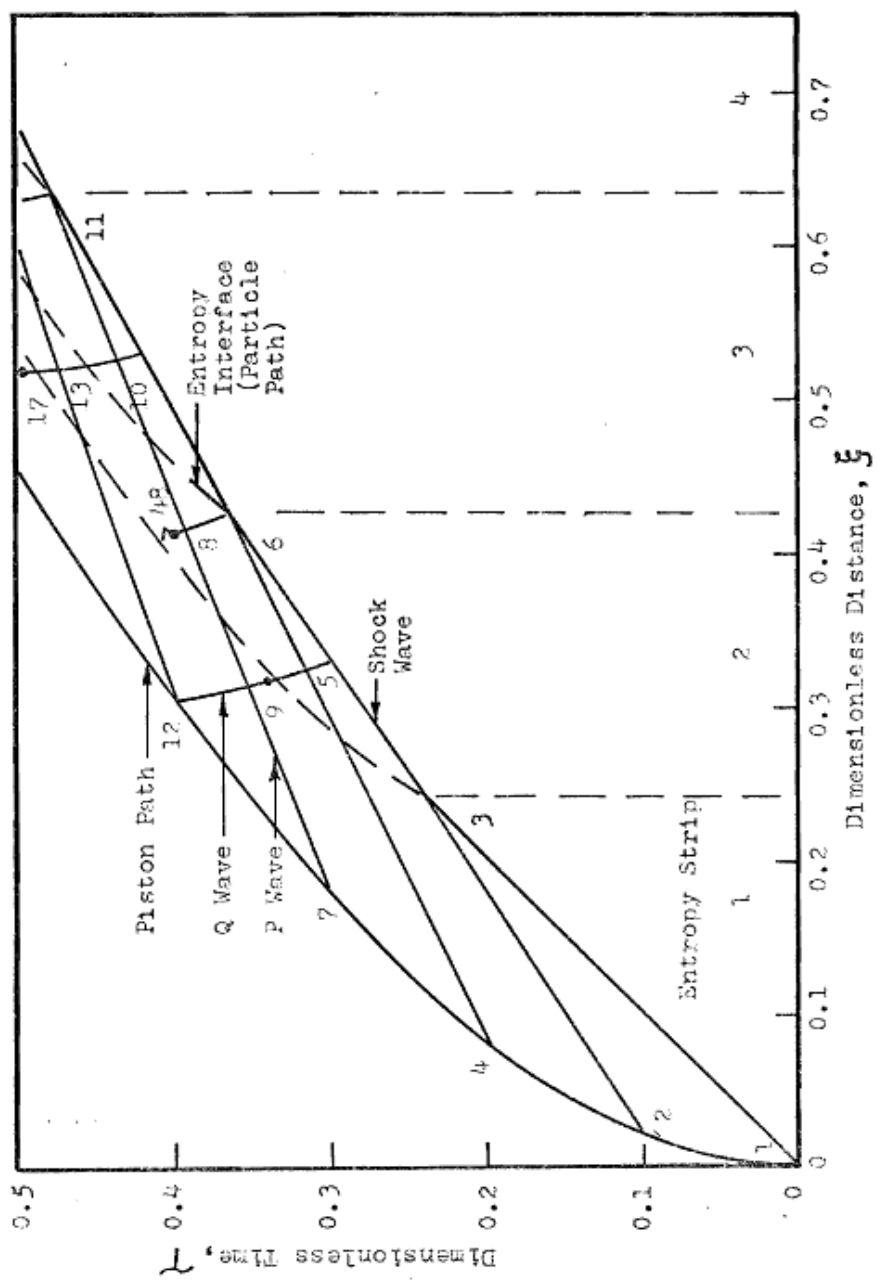

Figure 3.7 Wave diagram for a 1-D accelerating piston.

Several shockwave characteristics can be estimated by using the plot above and substituting the proper characteristic time and length dimensions for the current experiment. Doing so yields a shock formation time of 40 ns and a standoff distance of 12.5 μm. Therefore, it is expected that detached shock waves will form well before any droplet breakup. However, the acceleration experienced by the actual droplets is greater than the theoretical acceleration used in

this solution so it is likely that the shock formation time and standoff distance will be somewhat smaller than predicted. Also, note that the droplet can move as much as 12 μm during image acquisition so some blurring may occur. These difficulties complicate the quantitative determination of actual thickness and standoff distance but nonetheless, provide a useful indication of the qualitative trends.

The method of characteristics can be refined using the time and relative Mach number versus downstream distance reported by Kim & Hermanson [10]. Plots of droplet dynamics as shown by the downstream (*z*-position) versus time and relative Mach number are shown in Fig. 3.8; the underlying position-time data are shown in Fig 3.9 [10].

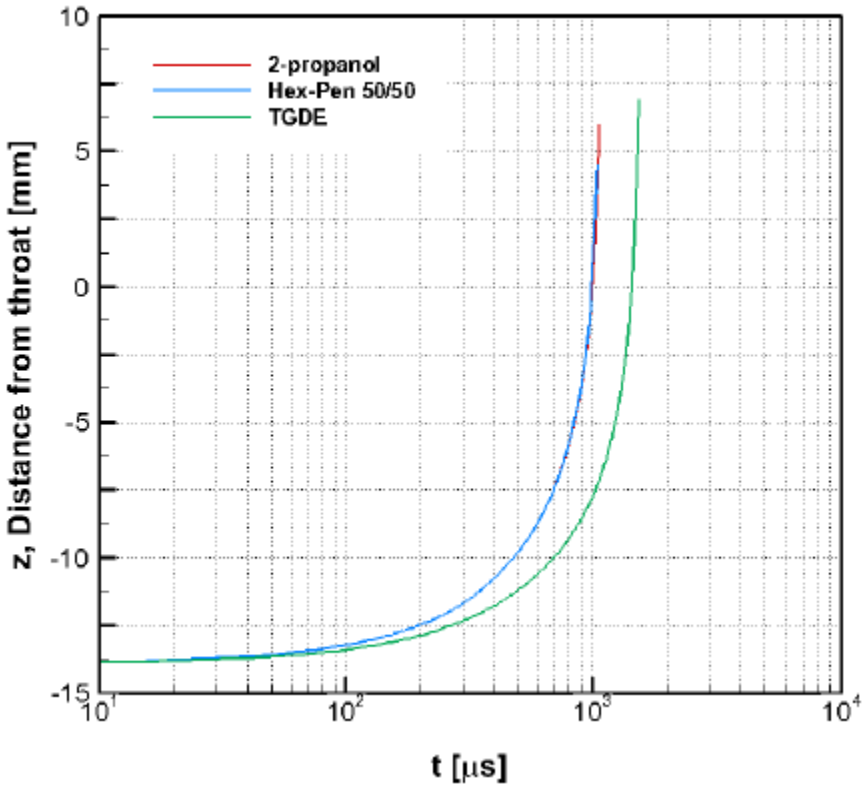

Figure 3.8 The change in droplet position with time [10].

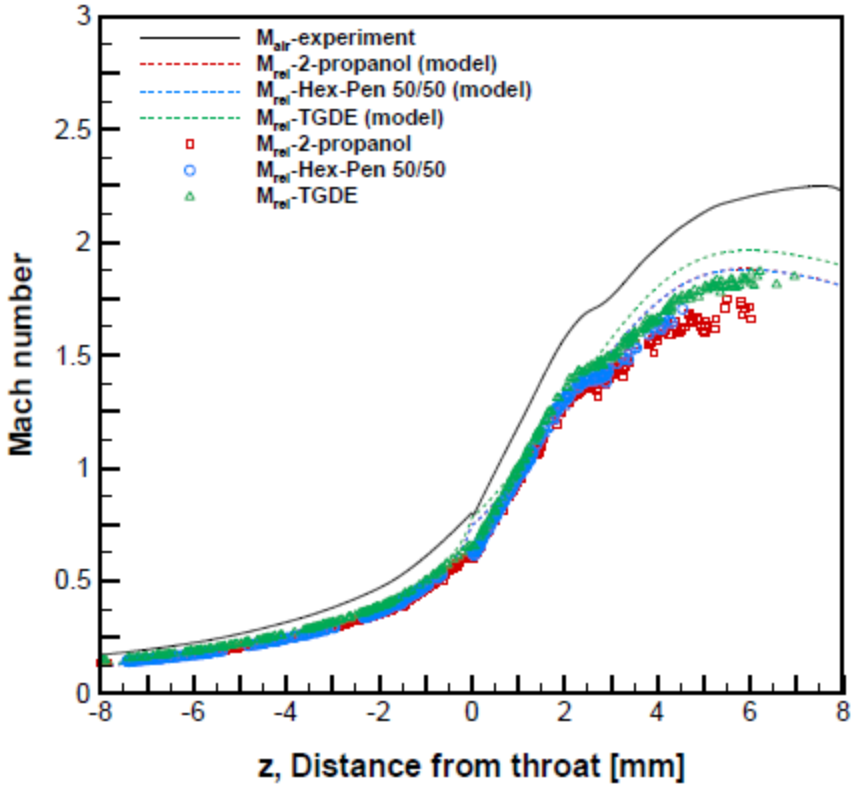

Figure 3.9 The evolution of relative Mach number with position [10]. Results for 2-propanol droplets are shown with red symbols.

The same Riemann variables are used to find the physical characteristics and to plot wave paths. A shock wave forms at the point wave paths begin intersecting and the shock formation time, as well as standoff distance, can be estimated. The wave diagram for the accelerating droplet is shown below in Fig. 3.10.

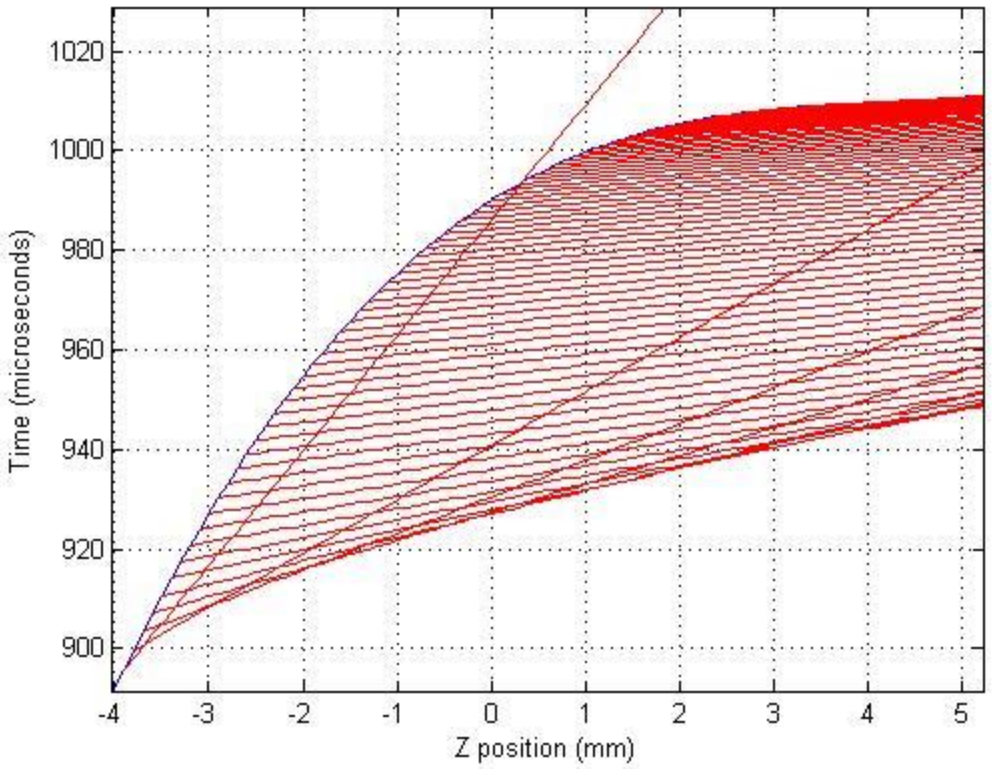

Figure 3.10 Wave diagram for an accelerating droplet.

Based on the plot above, the expected standoff distance is 14 μm and the corresponding formation time is 1300 ns. Compared to the accelerating piston case discussed previously, the predicted values are ~1.12 times greater for standoff distance and ~32.5 times greater for shock formation time. Based on the number of converging waves, it is expected that a shock has formed by the time the droplet is 2 mm downstream of the throat which corresponds to a time of approximately 1 ms after injection. Both of these values are within the typical droplet path and lifetime. The differences are likely due to the fact that the accelerating piston case discussed previously experiences relatively steady acceleration compared to the actual droplets which experience relatively unsteady acceleration.

One additional way to approximate the expected bow shock standoff is to apply results from bluff nosecone studies steady supersonic flow. Inger [14] studied how the standoff distance

varied with the shock layer Reynolds number. The shock layer Reynolds number is calculated using bow shock thickness rather than the droplet diameter as the characteristic length; based on the predicted shock thicknesses obtained from the Mott-Smith solution, the maximum shock layer Reynolds number is 11 for this research. A plot describing the behavior of non-dimensionalized standoff distance is shown below [14].

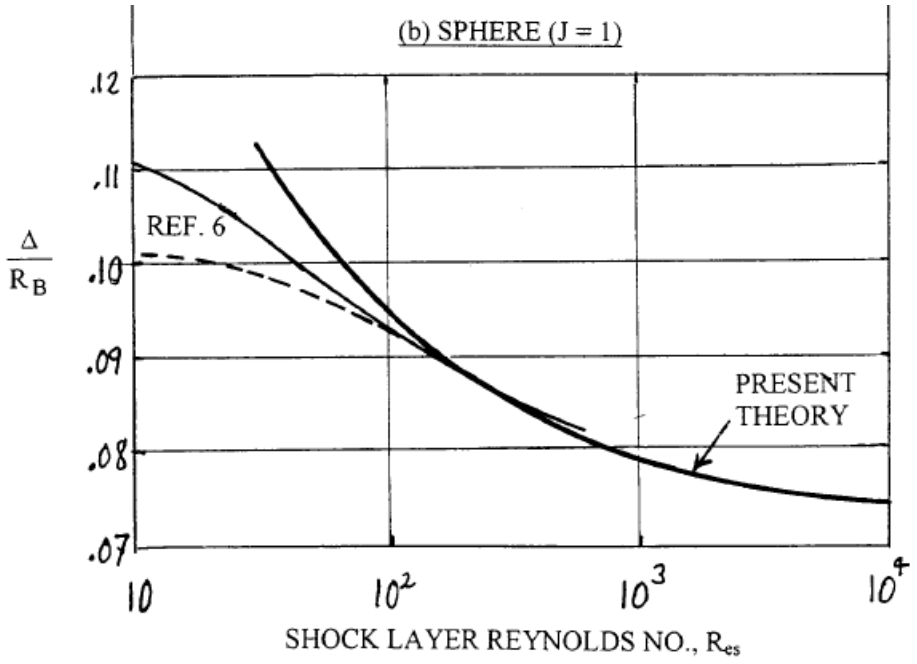

Figure 3.11 Non-dimensionalized shock standoff distance.

In Fig. 3.11, Δ represents the standoff distance, R_B is the radius of the body, and R_{es} is the shock layer Reynolds number. Using Inger's results, the bow shock standoff distance is expected to be approximately 0.11 times the droplet radius, or approximately 5.5 μm. Therefore, the expected range for standoff distance is in between 5.5 and 14 μm. It is possible that the standoff distance will be on the lower end of the estimated range due to the expected increase in pressure behind the bow shock that may "push" the deforming droplet toward the bow shock and decrease the standoff distance.

An additional characteristic of interest is the time it takes for a bow shock to react to droplet deformation. The time for a bow shock in front of a droplet to react to droplet deformation can be expected to be equivalent to the time it takes for information to propagate from the droplet back to the bow shock. This can be expressed as:

$$t_{reaction} = \frac{\Delta}{a} \qquad \text{Equation 3.6}$$

where Δ represents the standoff distance and a is the local speed of sound. However, speed of sound is not constant and depends on the local static temperature, which varies with the freestream Mach number. Use of the following isentropic normal shock equations allows for determination of the reaction time.

$$\frac{T_1}{T_0} = \frac{\{[2\gamma {M_1}^2 - (\gamma - 1)][(\gamma - 1){M_1}^2 + 2]\}}{(\gamma + 1)^2 {M_1}^2} \qquad \text{Equation 3.7}$$

$$a = \sqrt{\gamma R T} \qquad \text{Equation 3.8}$$

where T is the static temperature, R is the universal gas constant divided by the molecular weight of the gas, M_1 is the freestream Mach number, and γ is the ratio of specific heats.

Based on a predicted maximum standoff distance of 14 μm, the bow shock reaction time is expected to be between 33.0 ns and 40.7 ns for the current investigation, depending on the relative Mach number. The characteristic time for droplets to deform enough to transition into different deformation regions is roughly 0.02 ms, or 20,000 ns. The bow shock reaction time is at most 0.20% of the droplet deformation time, so it is expected that bow shocks accommodate very quickly to a deforming droplet.

When droplets reach relatively supersonic speeds, they are primarily in Region II and still maintain a fairly spherical front so bow shocks are expected to be similar in appearance to the

one shown in Fig. 3.12 below [15]. As droplets deform more significantly, such as those in Region III and IV (shown above in Table 2.1), they do not necessarily maintain a spherical front. Droplets with a more bluff-shaped windward surface may be expected to produce accompanying bow shocks similar to the one shown in Fig. 3.13 below [15].

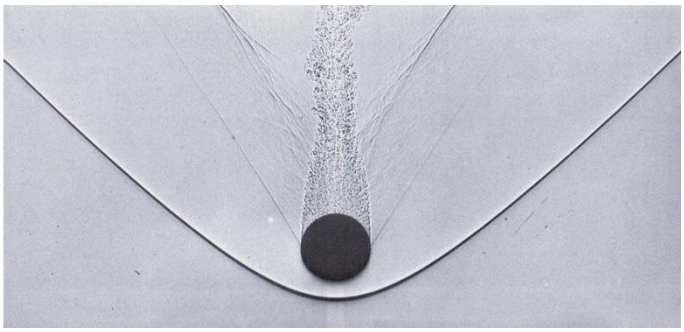

Figure 3.12 Bow shock in front of a sphere at M = 1.36.

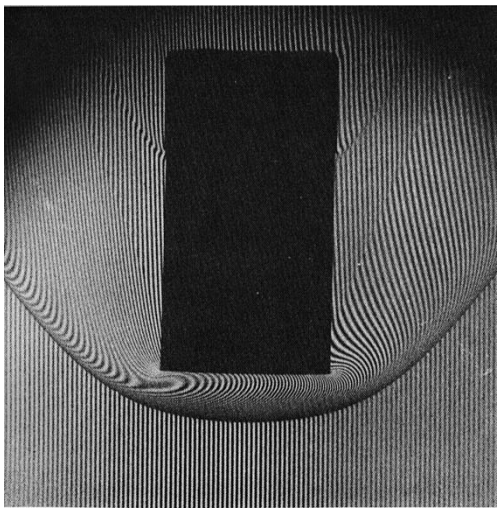

Figure 3.13 Bow shock in front of a bluff body at M = 2.77.

3.5 Schlieren Imaging of Disrupting Droplets

As mentioned previously, schlieren imaging was performed in order to visualize the bow shock in front of the droplet. The bow shocks appear as curved lines in front of the droplets and have varying degrees of opacity depending on the density gradient at that point. Also, the bow shocks occasionally appear darker on one side than the other. Possible explanations of this may

include orientation of the shock relative to the fixed knife edge and asymmetry associated with droplet deformation. The results are classified into the deformation regions defined by Kim & Hermanson [7,8,10] and presented below. There is some uncertainty associated with defining the deformation region to which each droplet belongs, especially given the rather limited data set. Over 17,000 images were taken as part of this investigation. The difficulties in capturing droplets stem largely from uncertainties in their position relative to the imaging region. The following discussion roughly follows the regions previously identified by previous research. Note that there are no results for Region I as the relative Mach numbers for that region are subsonic.

3.5.1 Region II Schlieren Images

In Region II, which typically occurs between -2 and 0 mm downstream of the throat, the droplets were relatively transonic or just relatively supersonic for the flow configuration achieved in experiment. Based on the theoretical predictions described above, it is expected that the bow shock will be approximately 15 to 20 times the mean free path in thickness, where the mean free path is approximately 40 nm. The corresponding bow shock standoff distance would be between 5.5 μm and 14 μm. Also, the bow shocks should appear similar to bow shocks in front a sphere due to the fact that the windward side of the droplet remains spherical despite the deformation. The schlieren images corresponding to this region of deformation are shown below in Fig. 3.15. In these images, both the flow direction and droplet motion is from the bottom up.

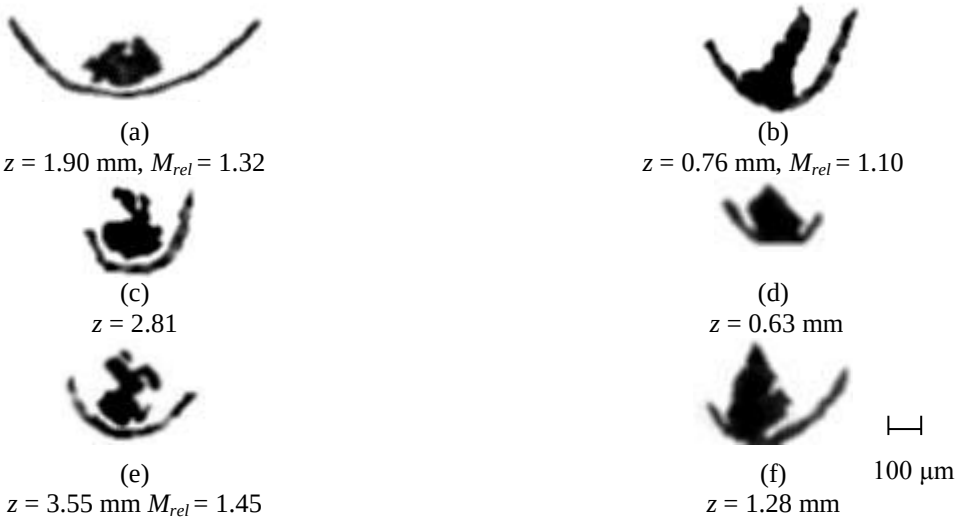

Figure 3.15 Schlieren images for Region II.

As expected, the physical appearance of the bow shock is similar to those in front of a spherical obstruction. All bow shocks detected are facing the incoming flow, meaning they are consistent with the orientation of the flow and behaving as expected for supersonic relative Mach numbers. In Fig. 3.15 (b), (d), and (f), there is no noticeable standoff distance between the bow shock and the droplet presumably due to exposure-time blurring. As discussed earlier, this blurring somewhat complicates the accurate measurement of thickness and standoff distance. However, there are several measurements that can be made in order to verify that the bow shocks shown truly are bow shocks. For example, that the measured blurred shock thickness exceeds the expected blurring due to the finite exposure time mentioned previously lends confidence towards the confirmation of bow shock existence. Additionally, if the captured bow shock extends sufficiently far, the Mach angle can be measured and used to calculate the relative droplet Mach number for comparison to known values. Table 3.4 below is a summary of the measured and predicted bow shock characteristics for Fig. 3.15 (a), (b), and (e). The estimated uncertainty associated with these measurements is typically less than 15%.

Shock Characteristic	(a)	(b)	(e)
Measured Mach Angle	49.3˚	64.7˚	43.3˚
Measured *z*-position	1.9 mm	0.76 mm	3.55 mm
Expected Mach #	1.25	0.88	1.50
Calculated Mach #	1.32	1.10	1.45
Deviation	5.3%	20.0%	3.4%
Predicted Thickness	12.8 μm	14.7 μm	12.6 μm
Measured Thickness	16.7 μm	19.2 μm	22.4 μm
Deviation	23.4%	23.4%	43.8%

Table 3.4 Bow shock characteristics for Region II.

The measured and expected Mach numbers for the droplets shown in Fig. 3.15 (a) and (e) are within several percent of each other. Kim & Hermanson's [10] relative Mach number data, shown in Fig. 3.9 above, shows that it is possible for the relative Mach number to vary between 0.1 and 0.2 depending on the distance downstream of the throat. However, for the droplet shown in Fig. 3.15 (b), there is a significant difference between the calculated and expected Mach numbers. Most significantly, based on the Mach angle, the droplets can be supersonic where they are generally expected to be subsonic.

This is an outlier compared to Kim & Hermanson's [10] results, but for this experiment, only supersonic outliers in the subsonic region were recorded. Otherwise, if the droplet was subsonic, there would be no bow shock and the resulting image would be irrelevant for this research. A possible explanation for why these outliers exist is that the initial droplet may have been larger than ideal, which means it accelerated less rapidly, resulting in a greater relative Mach number. Additionally, the droplets may have deformed in an unusual way that caused it to lag the flow more. As mentioned above, the relative Mach numbers have been observed to vary between 0.1 and 0.2 from the recorded value depending on the distance from the throat. Also, these relative Mach number expectations from the results of Kim are for droplets directly on the centerline of the test section. CFD analysis performed by Kim [8] show that the flow is non-uniform across the test section and may vary as much as 0.03 in flow Mach number depending

on how far off the centerline the droplet is. These factors combined may cause both the droplet and air flow velocities to vary, resulting in a higher relative Mach number in some cases.

The bow shock thicknesses were also measured and compared to the expected thicknesses, taking into account the presence of image blurring. For the images in Fig. 3.15 (a), (b), and (e), all of the measured thicknesses were greater than the predicted thicknesses which confirms that what was being observed are likely bow shocks. Additionally, the measured bow shocks grow rather than shrink in thickness as the droplet travels downstream, which suggests that more blurring has occurred. This is consistent with droplet acceleration with downstream distance.

3.5.2 Region III Schlieren Images

In the third region of deformation, typically occurring between 0 and 3 mm downstream of the throat, a portion of the droplet fluid begins separating from the rest of the droplet, typically forming a tail. Additionally, the droplets' windward-fronts no longer necessarily remain symmetric. As discussed previously, it is expected that the bow shock reaction time is shorter than the deformation time by several orders of magnitudes so that the bow shock will be able to quickly react to the deforming shock. This suggests that for the case of asymmetric droplet fronts there should be an asymmetric bow shock and for droplets with a symmetric and bluff front, there should be a corresponding bluff bow shock, as suggested by Fig. 3.13. Schlieren images for Region III are shown below in Fig. 3.16.

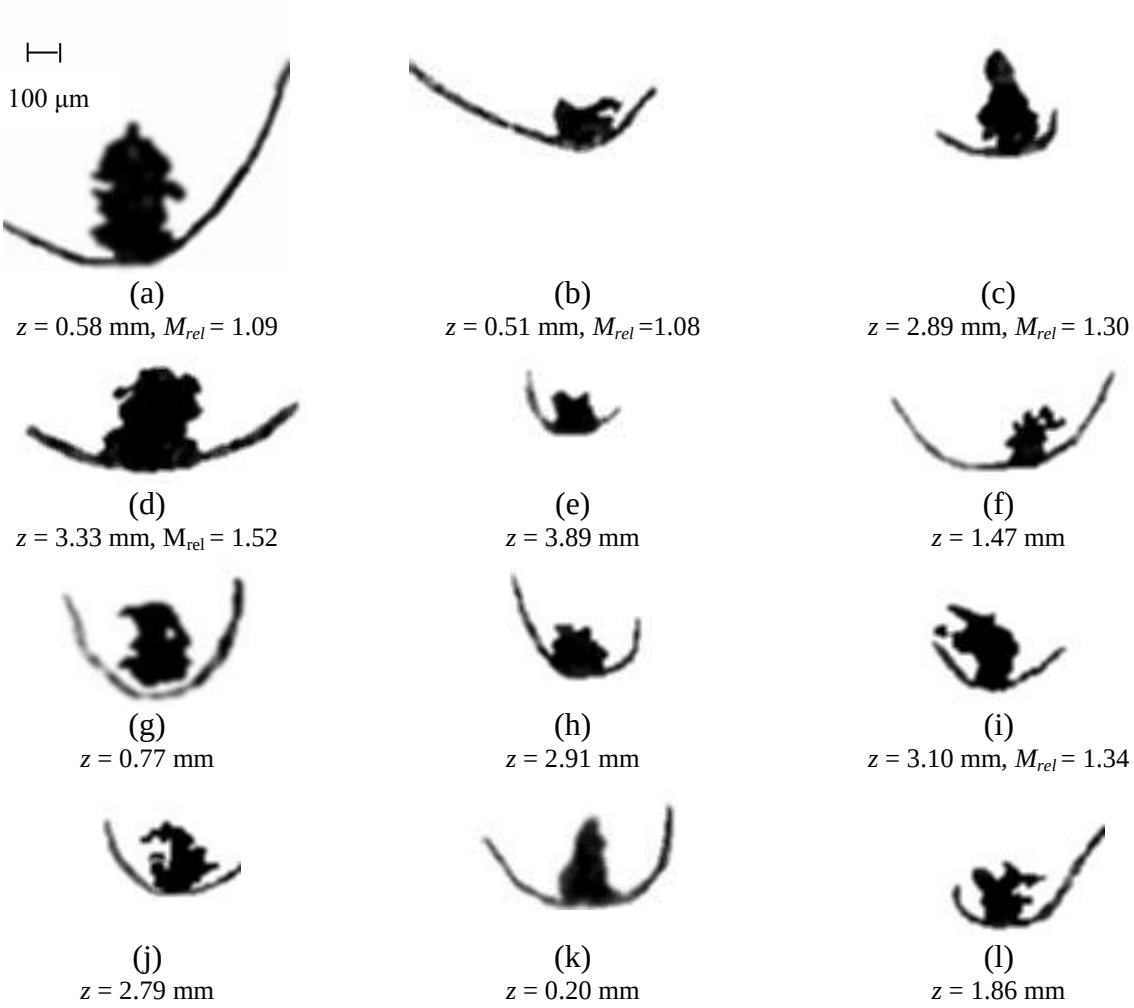

Figure 3.16 Schlieren Images for Region III.

The orientations of the droplets and accompanying bow shocks are consistent with what was seen in Region II and what is expected based on the flow direction. The bow-shock patterns here also appear to be consistent with the shock reaction time being less than the droplet deformation time. Droplets that appear symmetric (b, d, g in Fig. 3.16) have fairly symmetric bow shocks, droplets with asymmetric fronts (a, l) have asymmetric bow shocks, and droplets with bluff fronts (d, e, m) appear to have bluff bow shocks. If, on the other hand, the bow-shock reaction time was greater than the droplet deformation time, the bow shocks could be expected to retain a more symmetric and rounded form regardless of droplet deformation. The shock patterns in Fig. 3.16 (a), (f), and (j) also suggest that the flow in the test section is not purely in the

z-direction because the normal of the bow shocks appears to be oriented slightly sideways. This is consistent with previous CFD simulations of the flow field which indicated a degree of non-uniformity in the flow [8].

The measurements of bow shock thickness and Mach angle are repeated for Region III using the droplets shown in Fig. 3.16 (a), (b), (c), (d), and (i). The measurements are summarized below in Table 3.5.

Shock Characteristic	(a)	(b)	(c)	(d)	(i)
Measured Mach Angle	66.1˚	67.7˚	50.1˚	41.0˚	48.4˚
Measured *z*-position	0.58 mm	0.51 mm	2.89 mm	3.33 mm	3.10 mm
Expected Mach #	0.8	0.75	1.35	1.45	1.38
Calculated Mach #	1.09	1.08	1.30	1.52	1.34
Deviation	26.6%	30.6%	3.8%	4.6%	3.0%
Predicted Thickness	15.28 μm	15.34 μm	13.0 μm	13.6 μm	13.0 μm
Measured Thickness	16.9 μm	15.9 μm	17.7 μm	29.8 μm	19.6 μm
Deviation	9.6%	3.5%	26.6%	54.4%	33.7%

Table 3.5 Bow shock characteristics for Region III.

Again, there are droplets that are supersonic based on Mach angle measurements, but are expected to be subsonic based on Kim's results for those cases closet to the nozzle throat. For droplets further downstream of the throat, such as (e) and (i), the calculated Mach numbers correlate well to the expected Mach numbers and are well within the expected range.

There are also significant deviations in the predicted and measure bow shock thicknesses. However, there is a definite trend where the apparent shock thickness grows as the downstream distance increases and this matches what was observed in Region II. As the droplets move downstream the relative Mach number increases and the apparent bow shock thickness decreases. In addition, the droplet velocity increases. The increased droplet velocity (and thus the increased amount of blur) is on the order of micrometers and likely masks the decrease in bow shock thickness, which is on the order of nanometers, if the Mott-Smith solution is applicable on this micro-scale.

Additionally, the shock standoff distance appears to decrease somewhat with increasing droplet deformation, as suggested by the results in Fig. 3.16 compared to the less deformed droplets in Fig. 3.15. This change in standoff distance might be expected as pressure changes associated with the bow shock lead to droplet deformation and the accompanying flow accommodation.

3.5.3 Region IV Schlieren Images

In Region IV, which typically occurs between 3 and 6.5 mm downstream of the throat, the relative droplet Mach number approaches its predicted maximum of 1.8 and there is total or catastrophic droplet breakup. At this point, there is generally no expected pattern or deformation mode. Schlieren images for Region IV are shown below in Fig. 3.17.

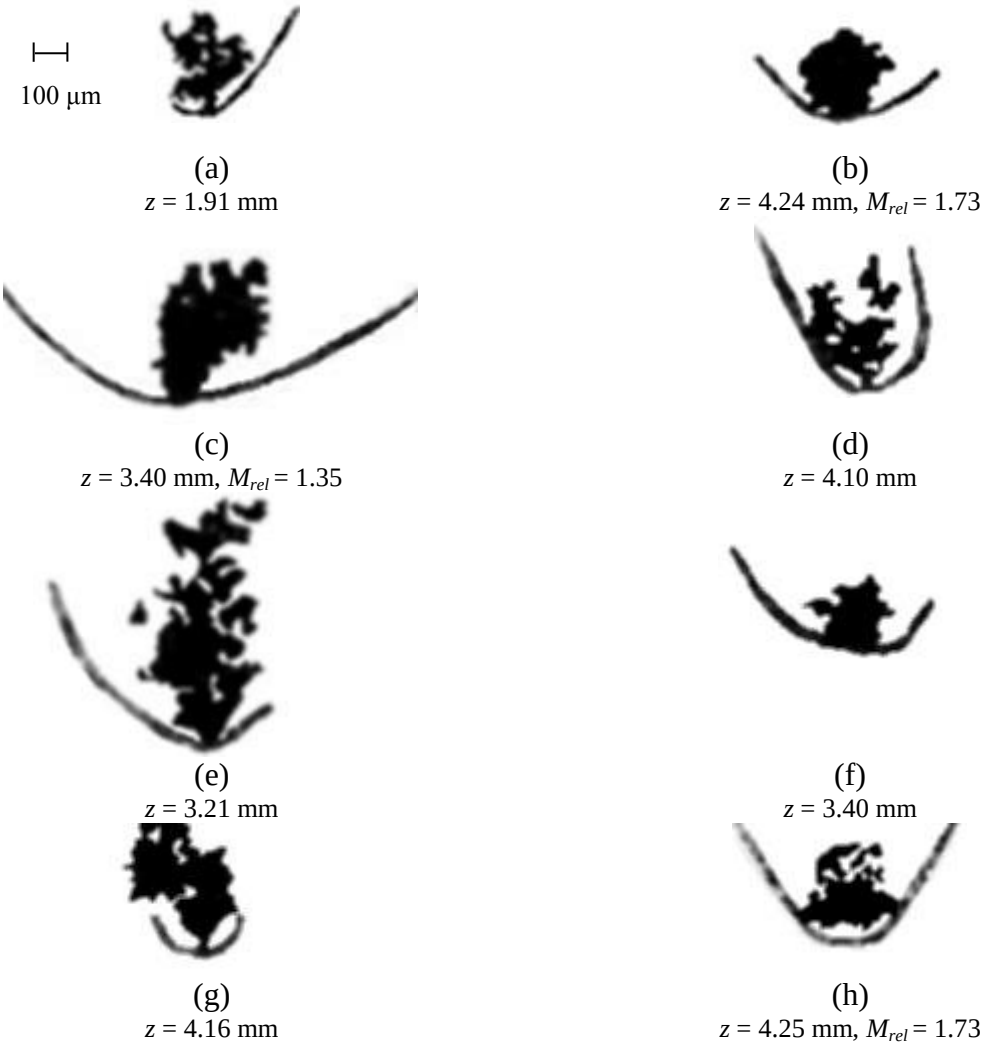

(a)
z = 1.91 mm

(b)
z = 4.24 mm, M_{rel} = 1.73

(c)
z = 3.40 mm, M_{rel} = 1.35

(d)
z = 4.10 mm

(e)
z = 3.21 mm

(f)
z = 3.40 mm

(g)
z = 4.16 mm

(h)
z = 4.25 mm, M_{rel} = 1.73

Figure 3.17 Schlieren images for Region IV.

The bow shock characteristics were measured for Fig. 3.17 (b), (c), and (h) and tabulated below.

Shock Characteristic	(b)	(c)	(h)
Measured Mach Angle	35.3˚	47.8˚	35.1˚
Measured z-position	4.24 mm	3.40 mm	4.25 mm
Expected Mach #	1.62	1.47	1.63
Calculated Mach #	1.73	1.35	1.73
Deviation	6.4%	8.9%	5.8%
Predicted Thickness	12.4 μm	12.8 μm	12.4 μm
Measured Thickness	26.5 μm	31.7 μm	35.4 μm
Deviation	53.2%	59.6%	65.0%

Table 3.6 Bow shock characteristics for Region IV.

The calculated Mach numbers correspond well with those measured previously in this flow configuration [10]. Also, Fig. 3.17 (b) and (h) have similar distances from the throat so it is reasonable to expect that they would have similar Mach numbers. The observed Mach numbers for (b) and (h) are consistent with each other based on the measured Mach angle. Additionally, the measured bow shock thickness follows the same trend as the bow shock thicknesses from Region III and Region IV. The calculated Mach numbers based on Mach angle throughout all regions are plotted against Kim's data, as shown below.

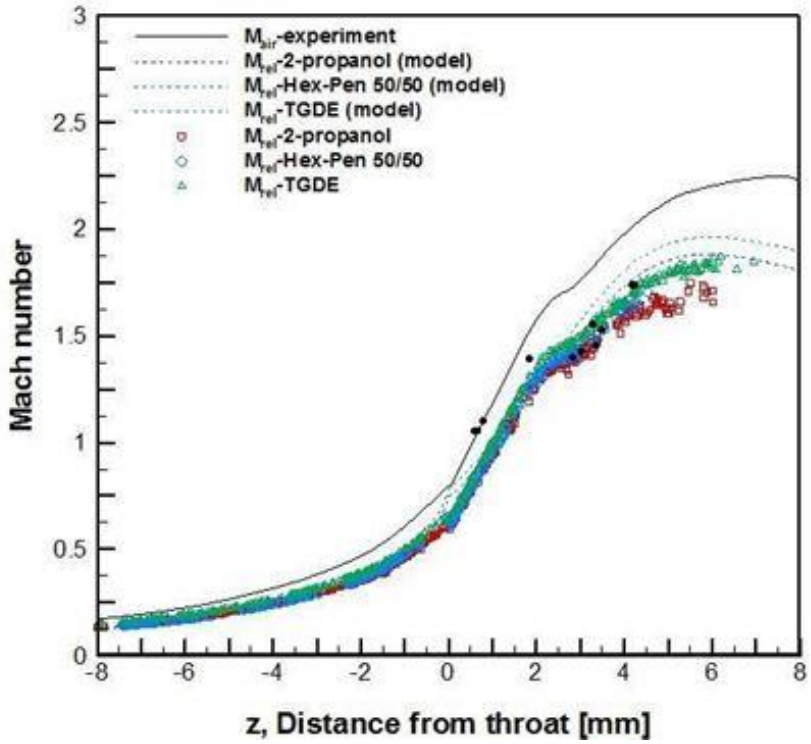

Figure 3.18 Relative Mach number variation with additional data points added.

3.6 Implications for Droplet Superheating

The static pressure was examined using the current results for relative Mach number. By using the normal shock equation for pressure rise on the centerline behind a detached bow shock,

the rise in static pressure can be estimated. The pressure behind a normal shock can be calculated by the standard relation:

$$p_2/p_1 = \left[1 + \frac{2\gamma}{\gamma + 1}(M_1^2 - 1)\right] \quad \text{Equation 3.9}$$

where p is the pressure, M_1 is the freestream relative Mach number, and γ is the specific heat ratio. If the supersonic outliers near the throat are taken into account, the static pressure may be up to 24.5% greater than previously estimated [7,8,10]. This increased static pressure could contribute to the suppression of superheat.

3.7 Summary Discussion

In summary, theoretical considerations suggest that it is possible for bow shocks to form on a time scale corresponding to the residence time of droplets under the flow conditions of this investigation. Bow shocks under these conditions were successfully imaged. The shocks were confirmed to be bow shocks by examining their behavior and examining several characteristics such as Mach angle and the apparent shock thickness. It was found that for droplets expected to be supersonic, the calculated Mach number correlated well with the predicted Mach number. However, droplets expected to be subsonic based on their downstream distance exhibited bow shocks in some cases and calculations based on the Mach angle associated with the bow shocks suggested that the droplets were supersonic relative to the surrounding air. These are outliers compared to previously established results, but in the context of this research, only supersonic outliers are relevant. Possible reasons that these outliers exist include the droplets had a slower velocity, leading to a higher relative Mach number, and inaccurate predictions due to the fact that Mach number can vary as much as 0.2 from the trendline.

Chapter 4 – Conclusions

1. The existence of bow shocks for droplets under locally supersonic conditions was confirmed by schlieren imaging.
2. Theoretical predictions for several bow shock parameters were made. The time scales of shock formation and shock reaction appear to be substantially less than the time scale of droplet disruption.
3. The bow shock patterns were observed to adjust to the deforming droplets which suggests that the shock reaction time scale is less than the time scale of droplet deformation. This is consistent with the theoretical predictions.
4. The Mach angle and the thickness apparent in the images were used to verify the presence of bow shocks. The Mach angles, in many cases, are consistent with the expected supersonic relative velocity, providing further confirmation of the detection of bow shocks around these droplets.

Chapter 5 – Recommended Future Work

The research presented here can be extended in several ways. First, it would be useful to repeat the direct imaging experiment with the alternative test fluids identified in order to test across a wider range of Weber numbers. Doing so may lead to a more complete determination of how droplet disruption and break up time depends on Weber number and relative Mach number. As a result, it may be possible to develop a scaling law that describes and predicts the break up behavior in this type of flow.

Second, the existence of bow shocks in front of micron scale droplets has been verified but the bow shock dynamics have not been fully characterized. By improving the sensitivity of the schlieren system and installing a more powerful light source, it may be possible to reduce the exposure time enough to improve the resolution of the bow shock structure. This would allow measurements of bow shock thickness, standoff distance, and if the exposure time is fast enough, shock formation and reaction time.

Finally, some interesting patterns were seen across several droplet fronts. In particular, the droplets in Fig. 3.15 (c) and (e), Fig. 3.16 (g), and Fig. 3.17 (h) all exhibited rippling across the droplet front. This interfacial instability of the disruption droplets should be examined in further detail. This would require extremely close-up imaging to capture the droplet front in enough detail.

Works Cited

[1] Colket, M. B., and L. J. Spadaccini. "Scramjet Fuels Autoignition Study." *Journal of Propulsion and Power* 17, no. 2 (2001): 315-323.

[2] Powell, O. A., J. T. Ewards, R. B. Norris, and K. E. Numbers. "Development of Hydrocarbon-Fuels Scramjet Engines: The Hypersonic Technology (HyTech) Program." *Journal of Propulsion and Power* 17, no. 6 (2001): 1170-1176.

[3] Sornek, R. J., R. Dobashi, and T. Hirano. "Effect of Turbulence on Vaporization, Mixing, and Combustion of Liquid-Fuel Sprays." *Combustion and Flame* 120, no. 4 (2000): 479-491.

[4] Krzeczkowski, S. A. "Measurement of Liquid Droplet Disintegration Mechanisms." *International Journal of Multiphase Flow* 6 (1980): 227-239.

[5] Hirahara, H., and M. Kawahashi. "Experimental Investigation of Viscous Effects Upon a Breakup of Droplets in High-Speed Air Flow." *Experiments in Fluids* 13 (1992): 423-428.

[6] Joseph, D. D., A. Huang, and G. V. Candler. "Vaporization of a Liquid Drop Suddenly Exposed to a High-Speed Airstream." *Journal of Fluid Mechanics* 318 (1995): 223-236.

[7] Kim, Y.J. and J. Hermanson. “Disruption of Volatile and Nonvolatile Droplets Under Locally Supersonic Conditions.” *AIAA Journal* 50 (2012) 1754-1765

[8] Kim, Y.J. “An Experiment Study of the Disruption and Vaporization of Non-Volatile and Volatile Droplets under Locally Supersonic Conditions.” PhD Dissertation, Department of Aeronautics and Astronautics, University of Washington, 2011

[9] Joseph, D.D., J. Ballanger, and G.S. Beavers. “Breakup of a Liquid Drop Suddenly Exposed to a High-Speed Airstream.” *International Journal of Multiphase Flow* 25 (1999): 1263-1303

[10] Kim, Y.J. and J. Hermanson. “Breakup and vaporization of droplets under locally supersonic conditions.” *Physics of Fluids* 24 (2012) 076102

[11] Hermanson, J. C. "Dynamics of Supersonic Droplets of Volatile Liquids." *AIAA Journal* 45, no. 3 (2007): 730-733.

[12] Vincenti, W., and C. Kruger. *Introduction to Physical Gas Dynamics*. 1st Edition. Malabar: Krieger Publishing Company, 1965. Print.

[13] Mann, M.J. “One-Dimensional Shock Wave Formation by an Accelerating Piston.” PhD Dissertation, Department of Aeronautical and Astronautical Engineering, Ohio State University, 1970.

[14] Inger, G. R. “Low Reynolds Number Effects on Hypersonic Blunt Body Shock Standoff.” 41st Aerospace Sciences Meeting and Exhibit, Reno, Nevada, January 6-9, 2003. American Institute of Aeronautics and Astronautics

[15] Van Dyke, M. *An Album of Fluid Motion.* 13th Edition. Stanford: The Parabolic Press, 2011. Print.

[16] Gerhauser, H., Hischmann, K., Lee, F., and Talke, F. "The Effect of Pulse Shape on the Drop Volume and the Frequency Response of Drop-on-Demand Ink Jet Transducers." *SID Digest* (1983): 110-110

Appendix A: Effect of Varying Waveform Parameters on Droplet Sizing

Droplet formation through piezoelectric jetting devices has been studied before but the focus of previous studies has been how different waveforms affect droplet formation. Garhauser, Hirschmann, Lee, & Talke [16] tested several waveforms, such as the square pulse, different sinusoidal pulses, and the error function. They discovered that the frequency response is independent of the waveform shape. Rather than testing various waveform shapes, the research presented here examines how varying individual parameters for a single waveform, the ramp pulse, will affect droplet formation. Only one waveform parameter was varied at a time and an optimal value was experimentally determined before testing the next parameter. The results for the waveform parameters are presented below in the order tested.

Pressure Variation

A fluid jet was formed without a signal from the droplet generator controller in order to isolate the effects of pressure. The pressures tested ranged from 7 kPa to 14 kPa. Sample images are shown below in Fig. A.1, with the pressure increasing from left to right.

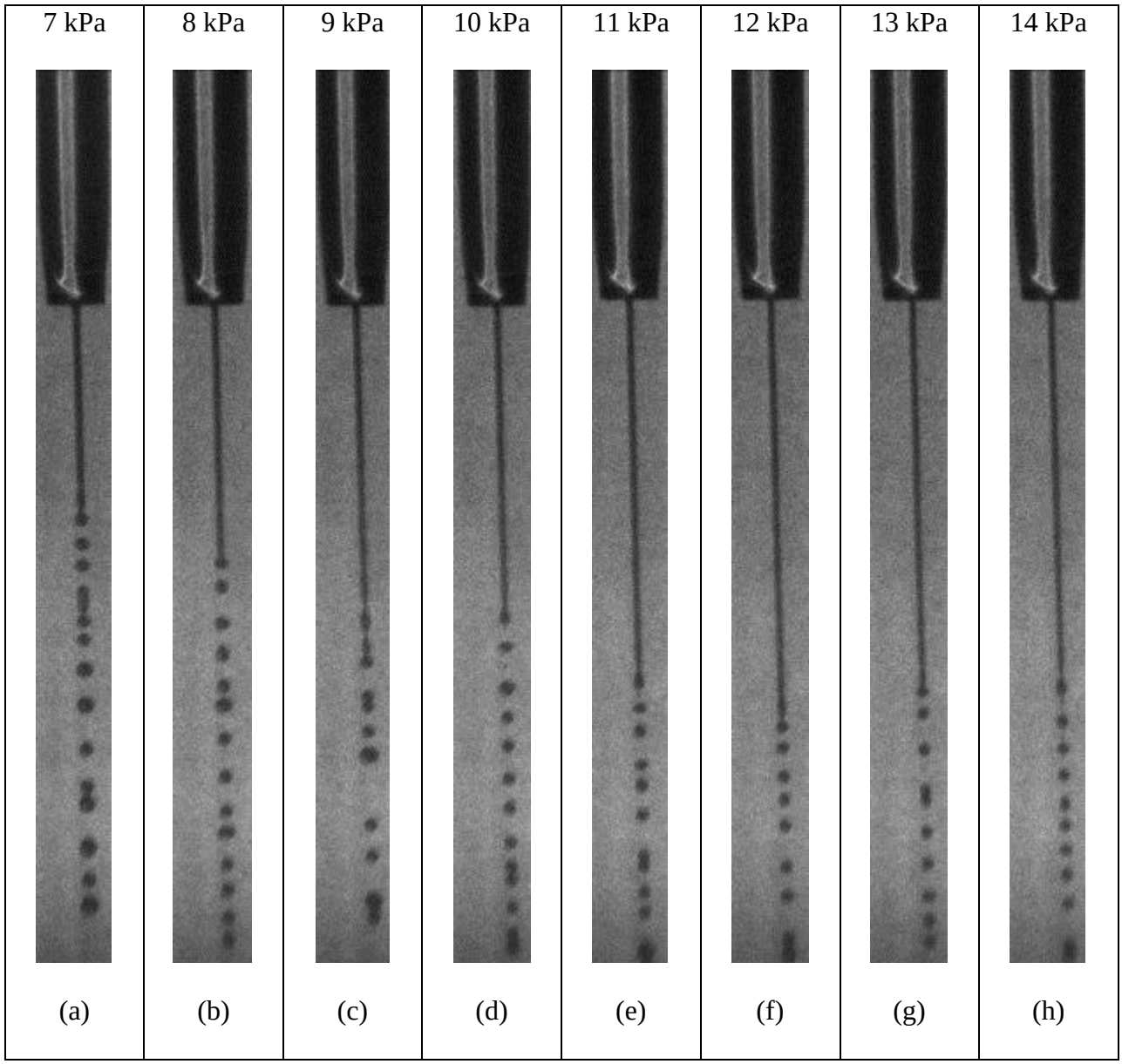

Figure A.1 (a)-(h) Fluid jet at different pressures.

It is evident that as the pressure is increased, there is also an increased delay time before the fluid jet begins breaking up due to instabilities. However, increasing pressure also increases

the jet velocity. This was not verified using a double exposure technique, but can be shown easily by applying Bernoulli's equation. Therefore, it is ideal to use the lowest pressure that still provides a jet, which is 7 kPa.

Frequency Variation

Next, the frequency was tested in 500 Hz intervals, starting from 0 Hz, until the desired droplet size was achieved. With a waveform being sent to the droplet generator, the fluid jet should breakup and form a stream of droplets. Sample images for frequencies between 2,500 Hz and 6,000 Hz are shown below in Fig. A.2, with frequency increasing from left to right.

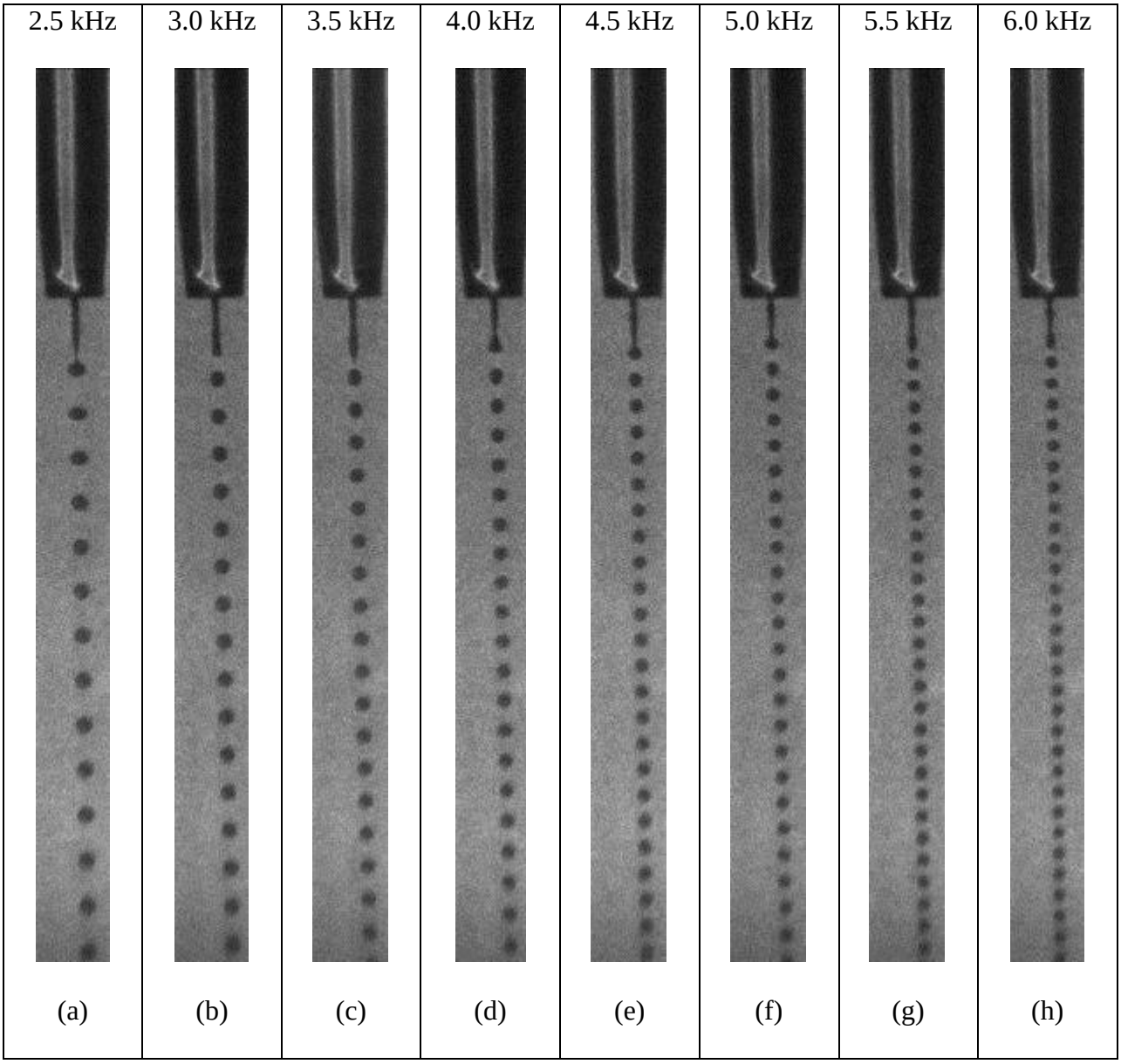

Figure A.2 (a)-(h) Droplet stream at different frequencies.

Based on Fig. A.2 (a) through (h), the effect of varying frequency is that as frequency increases, the droplet size decreases and additionally, the spacing between droplets decreases. Physically, these results make sense; increasing the operating frequency means the time interval between pulses decreases, so less time and fluid volume will pass between each pulse. At an operating frequency of 6,000 Hz, the droplets generated are consistently 100 ± 5 μm.

Voltage Variation

Voltage was the next waveform parameter tested. The initial voltage was 10 V and voltage was gradually increased by 1 V increments up to 30 V. Sample images for the voltage variations are shown below in Fig. A.3, with voltage increasing from left to right.

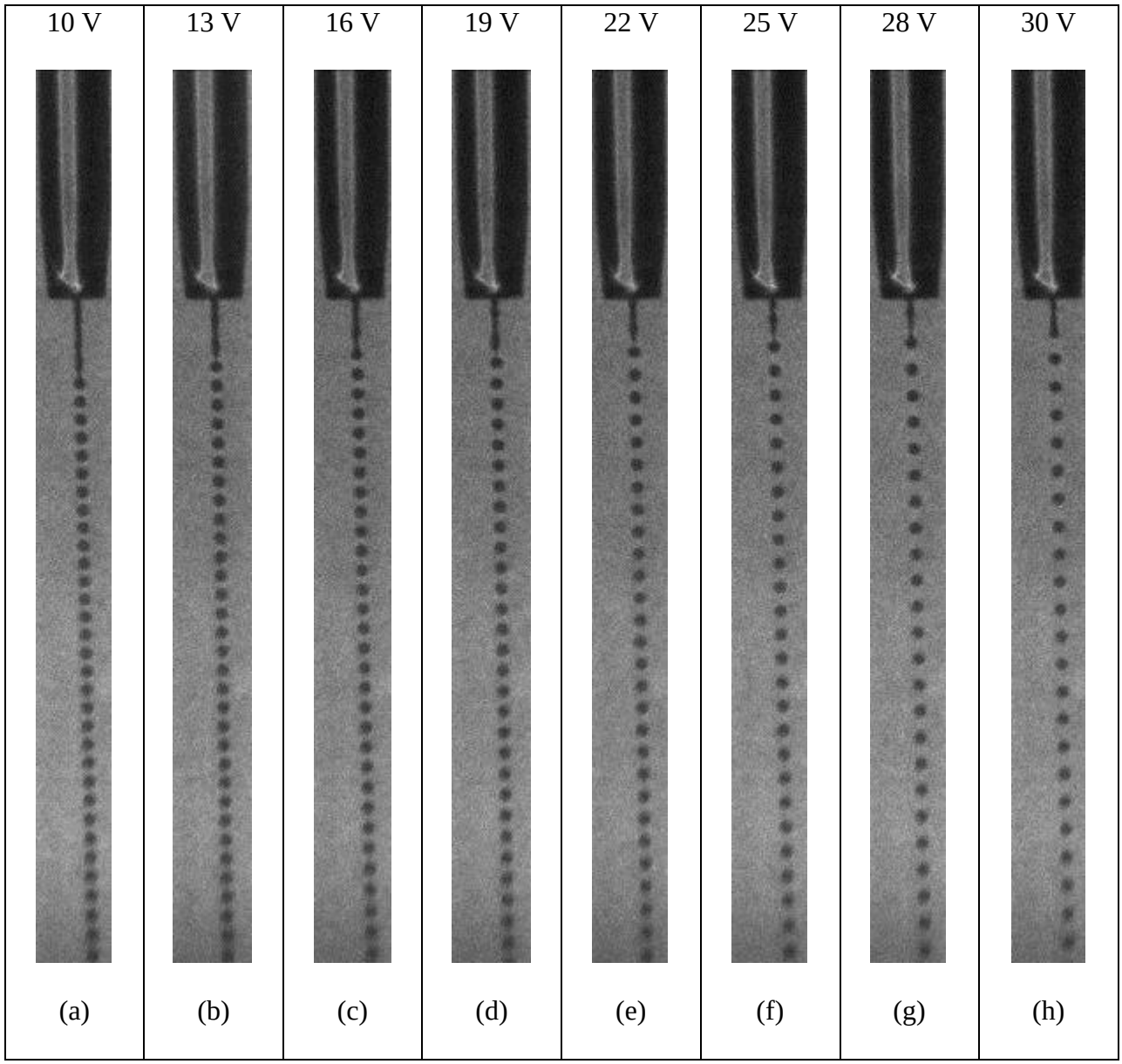

Figure A.3 (a)-(h) Droplet stream at different voltages.

Figure A.3 shows that as voltage is increased, the fluid jet breaks up into droplets sooner and the spacing between droplets increases. This suggests that as the waveform amplitude is

increased, the droplet velocity also increases. The waveform amplitude can be interpreted as energy input so it follows that a greater energy input (voltage) will lead to a greater energy output (faster droplets). In order to encourage faster droplet formation from the fluid jet while avoiding an increase in the initial droplet velocity significantly, 20 V was chosen as the ideal waveform voltage.

Dwell Time Variation

Next, the dwell time was tested. Based on the manufacturer's suggested settings the initial dwell time was set to 55 µs tested by increasing in 10 µs increments. Figure A.4 below shows sample images of the droplet stream at each dwell time.

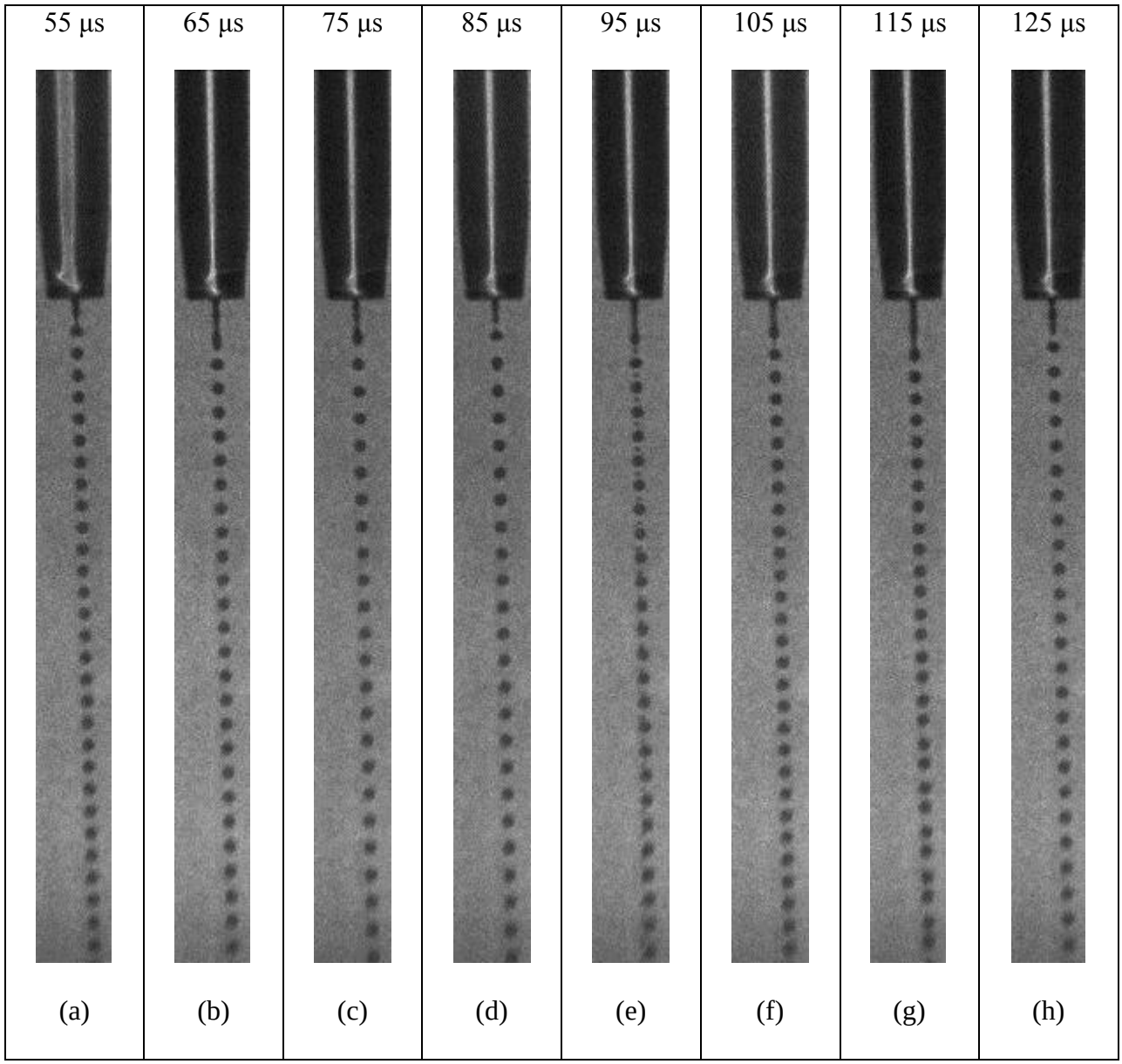

Figure A.4 (a)-(h) Droplet stream at different dwell times.

Both droplet shape and the spacing between droplets are affected by the dwell time. However, the primary concern is the appearance of satellite droplets, which is most evident in

Fig. A.4 (e). The effect of dwell time on droplet shape can be seen by comparing Fig. A.4 (d) and (h). In (d), the most recently formed droplets have a teardrop shape while in (h), the most recently formed droplets are spherical. This teardrop shape is also evident in (a) for the most recently formed droplet. While the droplets for all dwell times eventually become spherical, that may not be the case when the droplets are being injected into an accelerating flow instead of a static field. For this reason, the dwell time was chosen to be 125 μs as it has a consistent spherical shape and most importantly, no satellite droplets.

Rise and Fall Time Variation

Finally, the effect of rise and fall time was tested. Starting from the suggested rise and fall times of 2 μs, the rise and fall times were gradually increased in increments of 2 μs. Due to an imperceptible change from 2 μs to 10 μs, the step size was increased from 2 μs to 5 μs. Sample images of the droplet stream at different rise and fall times are shown below in Fig. A.5.

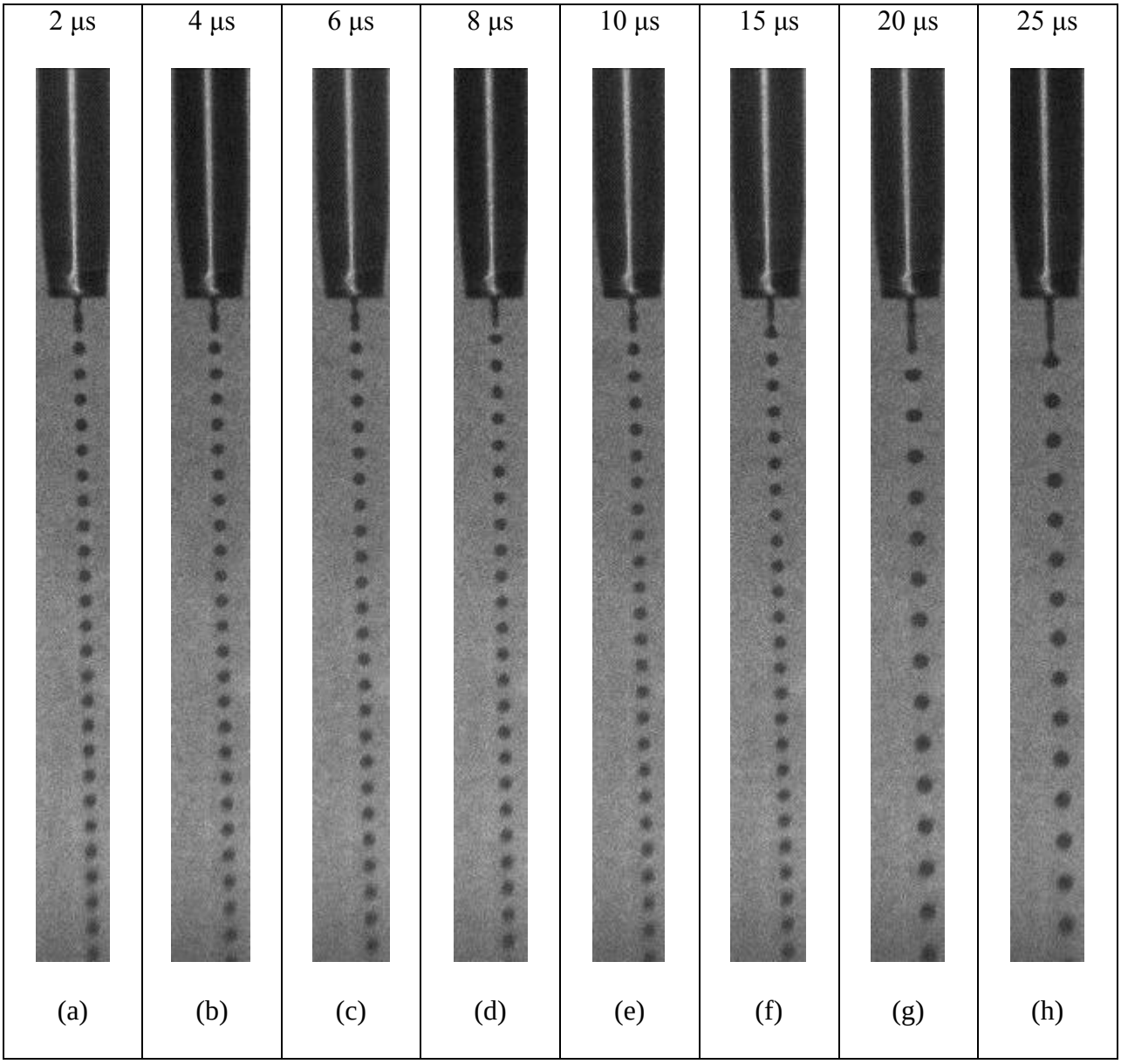

Figure A.5 (a)-(h) Droplet stream at different rise and fall times.

Based on Fig. A.5, rise and fall time can affect droplet size after it reaches a certain threshold. Between 2 μs and 15 μs, there is an insignificant change in droplet size but for 20 μs and 25 μs the droplets become significantly larger. The dwell time was kept at 125 μs and for the case of a 25 μs rise and fall time, the total waveform time becomes 175 μs, which is greater than the time allowed if the frequency is 6,000 Hz. The reason for the sudden increase in droplet size is most likely due to the fact that the operating frequency must decrease in order to meet the specified dwell, rise, and fall times. As long as the total wavepulse time does not exceed the time limit determined by operating frequency, there is no noticeable difference between different rise and fall times.

The final droplet parameters that were used for the research are: a rise and fall time of 5 μs, a dwell time of 125 μs, an operating frequency of 6,000 Hz, a voltage rise of 20.0 V, and a driving pressure of 7.0 kPa.

Appendix B: Alternative Test Fluids

Alternative Test Fluids for Superheat

In order to conclusively determine the effect of superheat, additional test fluids are needed. The primary considerations for alternative test fluids are their Ohnesorge number, surface tension, vapor pressure, and health risks. To test the effect of superheat, fluids with similar surface tensions but significantly different vapor pressures should be used. The previously tested fluids are shown below in Table B.1 [10].

Test Liquid	P_{vapor} (kPa)	ρ (kg/m^3)	μ (Pa s)	σ (N/m)	Oh
TGDE	0.0013	1384.66	0.003939	0.03385	0.05753
2-propanol	4.404	785.16	0.002311	0.02132	0.05649
Hexanol-Pentane 50/50	30.674	781.08	0.001345	0.02085	0.03332

Table B.1 Previously tested fluids.

Identifying fluids with similar characteristics except for vapor pressure is nontrivial so mixtures are also considered. Mixture properties are based on the volume of each fluid and were calculated using the software *Mixprops*. *Mixprops* uses the Soave modification of the Redlich-Kwong equation of state to perform calculations; vapor pressure was independently calculated using Raoult's law. The potential test fluids are given below in Table B.2.

Test Liquid	P_{vapor} (kPa)	ρ (kg/m^3)	μ (Pa s)	σ (N/m)	Oh
Acetone	46.4538	695.18	0.000322	0.02366	0.0079
Ethanol	11.0412	789.00	0.001074	0.02197	0.0258
Acetone-Ethanol 90/10	42.9125	711.00	0.000358	0.02355	0.0087
Acetone-Ethanol 80/20	39.3713	727.44	0.000399	0.02343	0.0097
Acetone-Ethanol 70/30	35.8300	744.53	0.000448	0.02332	0.0108
Acetone-Ethanol 60/40	32.2886	762.33	0.000506	0.02320	0.0120
Acetone-Ethanol 50/50	28.7475	780.88	0.000573	0.02308	0.0135

Acetone-Ethanol 40/60	25.2062	800.24	0.000654	0.02297	0.0153
Test Liquid	**P_{vapor} (kPa)**	**ρ (kg/m^3)**	**μ (Pa s)**	**σ (N/m)**	**Oh**
Acetone-Ethanol 30/70	21.6650	820.45	0.000751	0.02285	0.0173
Acetone-Ethanol 20/80	18.1237	841.59	0.000898	0.02274	0.0205
Acetone-Ethanol 10/90	14.5825	863.7	0.001010	0.02262	0.0229
Acetaldehyde	128.5877	648.00	0.000215	0.01762	0.0059
Acetaldehyde-2-prop 90/10	116.8131	683.87	0.000326	0.02037	0.0087
Acetaldehyde-2-prop 80/20	105.0386	707.38	0.000432	0.02048	0.0114
Acetaldehyde-2-prop 70/30	93.2641	731.33	0.000562	0.02060	0.0181
Acetaldehyde-2-prop 60/40	81.4896	755.77	0.000718	0.02071	0.0224
Acetaldehyde-2-prop 50/50	69.7151	780.74	0.000904	0.02082	0.0273
Acetaldehyde-2-prop 40/60	57.9406	806.29	0.001123	0.02094	0.0329

Table B.2 Alternative test fluids for superheat.

The fluids and mixtures shown above all have Ohnesorge number less than 0.1 and allow for various degrees of superheat. The lowest pressure reached in the test section is 10 kPa therefore the degree of superheat can be as high as 12.86 using Acetaldehyde. In previous experiments [10], superheat was only tested up to 3 degrees of superheat and contradictory results were found; by testing a significantly higher degree of superheat, superheat effects, if any, may be stronger and thus it may be possible to more conclusively determine the effects of superheat on droplet lifetime and breakup modes.

Alternative Test Fluids for Weber Number

The only fluid property that Weber number is dependent on is surface tension. Due to the inverse proportionality between Weber number and surface tension, fluids with less surface tension must be identified in order to test a wider range of Weber numbers. The potential test fluids are listed below from lowest to highest surface tension in Table B.3.

Test Liquid	P_{vapor} (kPa)	ρ (kg/m^3)	μ (Pa s)	σ (N/m)	Oh
Isopentane	96.94083	647	0.000214	0.01372	0.0077
1-Pentene	84.9475	661	0.000195	0.01545	0.0062
Pentane	70.2106	650	0.000224	0.01549	0.0072
Diethyl Ether	75.5607	734	0.000224	0.01665	0.0065
Isopropylamine	81.0237	72	0.000325	0.01680	0.0096
1-Hexene	25.0839	686	0.000252	0.01790	0.0072
Trichlorosilane	79.4148	1342	0.000326	0.01830	0.0066
2-Methyl-2-Propanol	6.1370	805	0.004312	0.01996	0.1008

Table B.3 Alternative test fluids for Weber number.

All but one of the eight fluids given in Table B.3 have vapor pressures greater than 10 kPa. 2-methyl-2-Proponol is the only non-volatile fluid but it has an Ohnesorge number that is slightly greater than 0.1, which is generally when viscosity is no longer negligible. However, due to the need to have a control fluid and the fact that the Ohnesorge number only exceeds 0.1 by 0.0008, 2-Methyl-2-Propanol remains a viable candidate for an alternative test fluid. The fluid with the lowest surface tension is Isopentane, with $\sigma = 0.01372$ N/m. Compared to Hexanol-Pentane 50/50, Isopentane has a 34.2% lower surface tension, so using Isopentane may increase the range of tested Weber numbers considerably.